Flexible routing of motor control signals through neocortical projection neuron classes

Junchol Park[1,†], James W. Phillips[1,2,†], Kathleen A. Martin[1,3], Adam W. Hantman[1], and Joshua T. Dudman[1,*]

[1] Janelia Research Campus, Howard Hughes Medical Institute, Ashburn, VA 20147
[2] Department of Physiology, Development and Neuroscience, University of Cambridge, UK
[3] *current address:* Center for Neural Science, New York University, New York, NY, USA
[*] *correspondence*: dudmanj@janelia.hhmi.org
[†] *equal contribution*

Motor cortex is part of a network of central brain circuits that together enable robust, flexible, and efficient movement in mammals. Recent work has revealed rich dynamics in mammalian motor cortex [1–7] thought to underlie robust and flexible movements. These dynamics are a consequence of recurrent connectivity between individual cortical neuron subtypes[8], but it remains unclear how such complex dynamics relate to individual cell types and how they covary with continuous behavioral features. We investigated this in mice, combining a self-paced, kinematically-variable, cortex-dependent, bimanual motor task [9,10] with large-scale neural recordings that included cell-type information. This revealed highly distributed correlates of movement execution across all layers of forelimb motor cortex and subcortical areas. However, we observed a surprising relative lack of modulation in the putative source of motor commands brain-stem projecting (pyramidal tract, PT) neurons [11]. By contrast, striatal/cortical projecting (intratelencephalic, IT) neurons showed much stronger correlations with movement kinematics. Cell-type specific inactivation of PT neurons during movement execution had little effect on behavior whereas inactivation of IT neurons produced dramatic decreases in the speed and amplitude of forelimb movements. PT inactivation elicited rapid, compensatory changes in activity distributed across multiple cortical layers and subcortical regions helping to explain minimal effects of inactivation on behavior. This work illustrates how cortical-striatal population dynamics play a critical role in the control of movement while maintaining substantial flexibility in the extent to which PT projection neurons are a requisite contributor to descending motor commands.

Introduction

The central control of movement is characterized by the ability to execute highly variable movements adapted to achieve diverse goals. For example, the same action can be executed at a continuously varying range or consistent vigor[12], utilize one or both forelimbs in a coordinated fashion[13], or be targeted to variable manipulanda[14]. The circuit mechanisms that underlie this remarkable flexibility while maintaining stable control of movement are difficult to understand[15]. On the one hand, flexibility could result from multiple distinct populations of projection neurons with specialized function[16,17] - although this raises questions about robustness since perturbation of a specific functional class should cause a specific functional deficit. On the other hand, it is possible that consistent dynamics[18] can be flexibly configured to use varying combinations of output pathways[5] - a proposal that can allow robustness against perturbation of a given cell type[19]. To date, there is data to both indicate relatively circumscribed functions of individual projection neuron classes and remarkable robustness to perturbation [20–23].

Motor cortex together with the subcortical striatum comprise the primary descending telecephalic circuits for the robust and flexible control of voluntary movements in vertebrates[24]. These forebrain pathways target multiple spinal projecting populations in the midbrain and brainstem which collectively are thought to control voluntary movements. Drawing upon insights from lesion studies and neuroanatomy, much work has suggested that motor cortex appears to play a role both in shaping dexterous movements that require fine articulation of the digits as well as the flexible adjustments of gross movements of the limb [11]. Classic studies have attempted to define the unique

contributions of cortex by studying tightly constrained tasks that tend to exhibit stereotyped and well-controlled movements of a limb, often about a single joint[25]. In diverse mammalian species these studies have revealed a clear functional representation of kinematics in single cortical neurons[26–28]. More recently, work has (re-)emphasized how these individual responses can also be viewed as components of collective population dynamics[7,29,30] that determine the preparation[31,32] and execution[1,2] of movement. To date, it remains unclear how population dynamics related to the control of voluntary movements map onto diverse motor cortical cell types.

It is generally thought that motor commands are carried by 'corticofugal' layer 5 pyramidal type (PT) neurons that project to multiple subcortical targets including the brainstem and spinal cord [11]. However, many studies have observed substantial movement execution related activity in other cell types throughout the motor cortex [3,26,33–35] raising questions about such a functional dissociation. The other major class of layer 5 output neuron, the intratelencephalic (IT) neuron, is also a major source of cortical input to striatum [26,36–38]. Basal ganglia, and striatum specifically [9,39], are also critical for controlling action and are closely associated with regulation of vigor during movement execution [24,40] putatively through descending projections to spinal-projecting premotor areas [40]. Moreover, corticostriatal projections from sensory areas are a critical component of action selection in the context of decision making tasks [41,42]. Thus, while motor commands are often argued to be carried primarily by PT neurons in mouse motor cortex[5,16,17], several lines of evidence indicate that movement-related activity is distributed across multiple cell types.

Here we sought to address these questions by combining large-scale neural recording across the entire motor cortical depth with genetic targeting and imaging of specific subpopulations of cortical neurons in the context of mice performing a flexible motor task. We find that IT neurons, but much less so PT neurons, have clear representations of movement execution and dominate the mode of population dynamics that represents kinematics. Closed-loop perturbation during movement execution revealed a critical dependence upon motor cortical activity for this task. However, cell-type specific perturbations revealed that the extent of PT neuron contribution to movement execution could be substantially altered without impairing robust control. These data suggest that the flexible routing of motor control signals through the major classes of projection neurons is critical for the robust neocortical control of movement.

Results

We examined neural dynamics during movement in mice using Neuropixels probes[43] that spanned all layers of neocortex and striatum. Mice were trained to make self-initiated (uncued) bimanual movements of varying amplitude to obtain delayed reward, similar to previously described tasks[9,39,43]. Briefly, head-fixed mice had to move a joystick past a threshold of varying amplitudes across three blocks to obtain a delayed water reward (Fig. 1A-B, Supplemental Video 1). Large scale recordings (384 sites) were used to record activity across all layers of forelimb motor cortex and throughout the dorsal and ventral striatum in behaving mice (Fig. 1A-I). Mice adjusted reach amplitude across blocks to efficiently collect rewards with individual movements (Fig. 1B, repeated measures ANOVA, $F_{2,14} = 7.94$, $p=0.006$, pairwise test, $p<0.05$).

A total of 1279 well-isolated single units were recorded across forelimb primary motor cortex ('$MCtx^{FL}$', N=599) and underlying striatum ('dSTR', N=680 units) (n=6 hemispheres, n=3 mice). Rich task-related neural dynamics were present. Population activity in both cortex and striatum peaked around movement. The temporally delayed (1 sec) reward in this task revealed prominent reward/consummatory tuning in ventral striatum as expected, but also revealed prominent reward-related activity in $MCtx^{FL}$ (Fig. 1C, F). Activity in a substantial fraction of $MCtx^{FL}$ units correlated with movement kinematics as previously described in dSTR for this task [9,39]. For example, many cortical units modulated their activity in proportion to the amplitude of the forelimb movement (Fig. 1D).

To quantify representation of reach amplitude by the $MCtx^{FL}$ neural population we used a targeted dimensionality reduction [44] method. Specifically, a simple linear regression was used to identify a dimension ($Dim^{amplitude}$) along which the $MCtx^{FL}$ population activity most covaried with forelimb movement amplitude (Methods). The population trajectories along this dimension differed

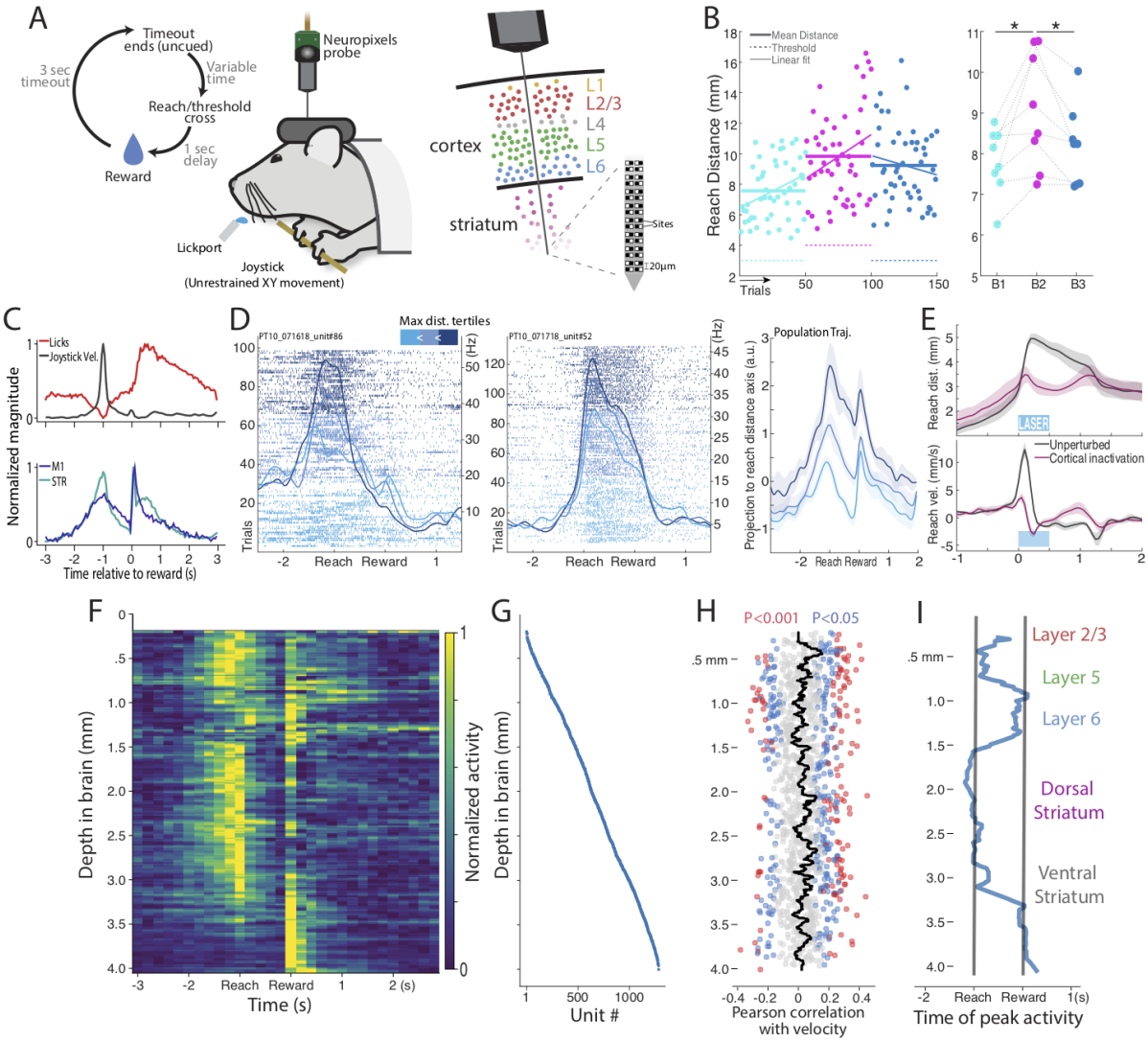

FIGURE 1
Distributed task related neural dynamics in a self-initiated variable amplitude operant task

A) Mice were trained to perform an self-initiated (uncued) vigor-control task, in which movements were made for delayed reward (left). To perform this, mice were head-fixed, and moved a joystick bimanually (middle). Recordings were made in forelimb motor cortex and striatum with a neuropixels 3A probe, which densely sampled neural activity in the depth axis (right, see inset for recording site spacing).
B) Mice adjusted their reach amplitude across the three blocks. Left plot shows data from a single session, right plot shows the data across sessions. See main text for statistics.
C) Population neural activity showed two peaks, one around reach and one around reward. Mean population activity relative to joystick velocity (thresholded to only show outward) and lick rate. Mean activity of units was taken for units above 1600um depth (cortical units) and those below 1800um depth (striatal units), then binned into 50ms bins, and each resulting array was normalized to the range 0-1.
D) Many units were tuned to movement kinematics. Two example units (left and middle) show tuning of neural activity to each tertile of reach amplitudes. Right figure shows neural population trajectories across the reach-amplitude tertiles acquired by projecting $MCtx^{FL}$ neural population activity onto the $Dim^{amplitude}$ dimension (see main text).
E) Brief closed-loop inactivation of $MCtx^{FL}$ neural activity by activation of inhibitory neurons in VGAT-ChR2 mice significantly reduced ongoing reach amplitude (top) and velocity (bottom), n=3 mice, 2 sessions/mouse.
F) Task-related neural activity was widely distributed across the depth of recordings. Mean activity at each depth from surface of the brain. Each row is normalized in the range 0-1.
G) Units were relatively evenly distributed across the recording depths.
H) Units that were significantly modulated by velocity were distributed across all cortical layers. Each dot is a single recorded unit. Plot includes all units in dataset. Values are Pearson's correlation coefficient and the corresponding p-value for each unit.
I) Time of peak activity shown by depth. Peak activity time was taken for each row in F, and the resulting array was smoothed with a savgolay filter with window length of 101 and polynomial order of 3.

significantly as a function of reach amplitude (Fig. 1D right, ANOVA, $F_{2,15} = 25.27$, $p = 1.57x10^{-5}$) indicating that $MCtx^{FL}$ neural activity in rodents is also tuned to continuous kinematic parameters of movement execution analogous to many previous reports in primate MCtx [27]. Previous work has demonstrated that basal ganglia activity plays a critical role in regulating movement execution in this task [9,10,39,40], thus we asked whether MCtx activity was also critical using a closed-loop optogenetic perturbation strategy. First, we used the initiation of a forelimb movement to trigger optical inactivation of MCtx using the VGAT-ChR2 mouse [45]. As in other forelimb tasks, *e.g.* joystick[46] or reach-to-grasp [47,48], we found that $MCtx^{FL}$ was critical for execution of a normal amplitude and speed movement (Fig. 1E, Supplemental Video 1; ANOVA, amplitude; $F_{1,10} = 11.33$, p=0.007; speed; $F_{1,10} = 47.55$, $p = 4.22x10^{-5}$). Closed-loop activation of descending output neurons from $MCtx^{FL}$ was also sufficient to invigorate movement (Supplemental Fig. 1A). Thus, these data provide evidence that MCtx activity is critical for controlling the vigor with which bimanual limb movements are executed.

Using our dataset with simultaneously recorded activity across all layers of MCtx and STR in behaving mice, we next examined the distribution of task related activity as a function of recording depth (Fig. 1F-I, Supplemental Fig. 1B). For example, regressing trial by trial activity of individual units with the speed of movement revealed significantly correlated units distributed relatively homogeneously throughout MCtx and dSTR (Fig. 1H). By contrast, units with predominantly movement-timed or reward-timed modulation of activity were not distributed homogeneously (Fig. 1I). In particular, reward-timed activity was most prominent in units recorded from ventral STR as expected. However, units recorded from depths corresponding to deep layer 5 in MCtx displayed delayed responses compared to units of upper or deeper layers (Fig. 1I). This observation was surprising. Deep layer 5 (putative layer 5b) is where the densest population of brainstem and spinal projecting PT neurons [11] are found in motor cortex. Brainstem projecting neurons have often been assumed to be the primary determinant of movement execution. In contrast, in this task, perhaps revealed by reward delivery delayed from movement execution, it appeared that reward-timed activity was more prominent in this putative PT population.

Given the apparent enrichment of reward-timed activity in units of putative layer 5b we next sought to more carefully characterize how activity related to task performance varied as a function of recording depth. We used an unsupervised dimensionality reduction approach (PCA) to extract the most prominent time-evolving patterns of $MCtx^{FL}$ activity. The top three principal components (PCs) explained on average 47±1.9% of the total variance across all datasets. Projection of $MCtx^{FL}$ population activity onto the first three PCs revealed population activity that peaked either early, up to 500ms after movement initiation (movement-timed), or later around the time of reward delivery (reward-timed), respectively (Fig. 2A). We next plotted the coefficients of these movement-timed and reward-timed PCs as a function of recording depth to examine whether these population activity dimensions were homogeneously distributed over recording depth (Fig. 2B-C). However, consistent with the characterization of individual unit activity previously (Fig. 1I), the movement-timed and reward-timed PC loadings were differentially distributed across the cortical depth as revealed by a significant interaction between group (movement-timed vs. reward-timed) and depth (Fig. 2D; Two-way ANOVA, $F_{1,31}=2.05$, $p=6.0x10^{-4}$, pairwise test, $p<0.05$).

While PT neurons are relatively concentrated at depths corresponding to deep layer 5, there is substantial heterogeneity in precise position of individual neurons[38]. To confirm that reward-timed responses were indeed observed in PT neurons we next sought to optogenetically "tag" PT neurons during recording[17,49–51]. We used expression of an optogenetic inhibitor of neural activity to identify putative PT neurons during recordings in behaving mice to mitigate against confounds due to recurrent excitation[49]. To achieve selective labelling of PT neurons a retrograde virus[52] with conditional expression of the inhibitory opsin FLInChR[53] was injected into the brainstem (pons) of Sim1-cre mice[54]. This strategy resulted in selective expression of an inhibitory opsin in pons-projecting PT neurons in M1 (Fig. 2E, Supplemental Fig. 2). A total of 111 units were putatively identified as 'tagged'; *i.e.* activity was significantly inhibited at short latency with half-maximal inhibition occurring 34±5 ms after

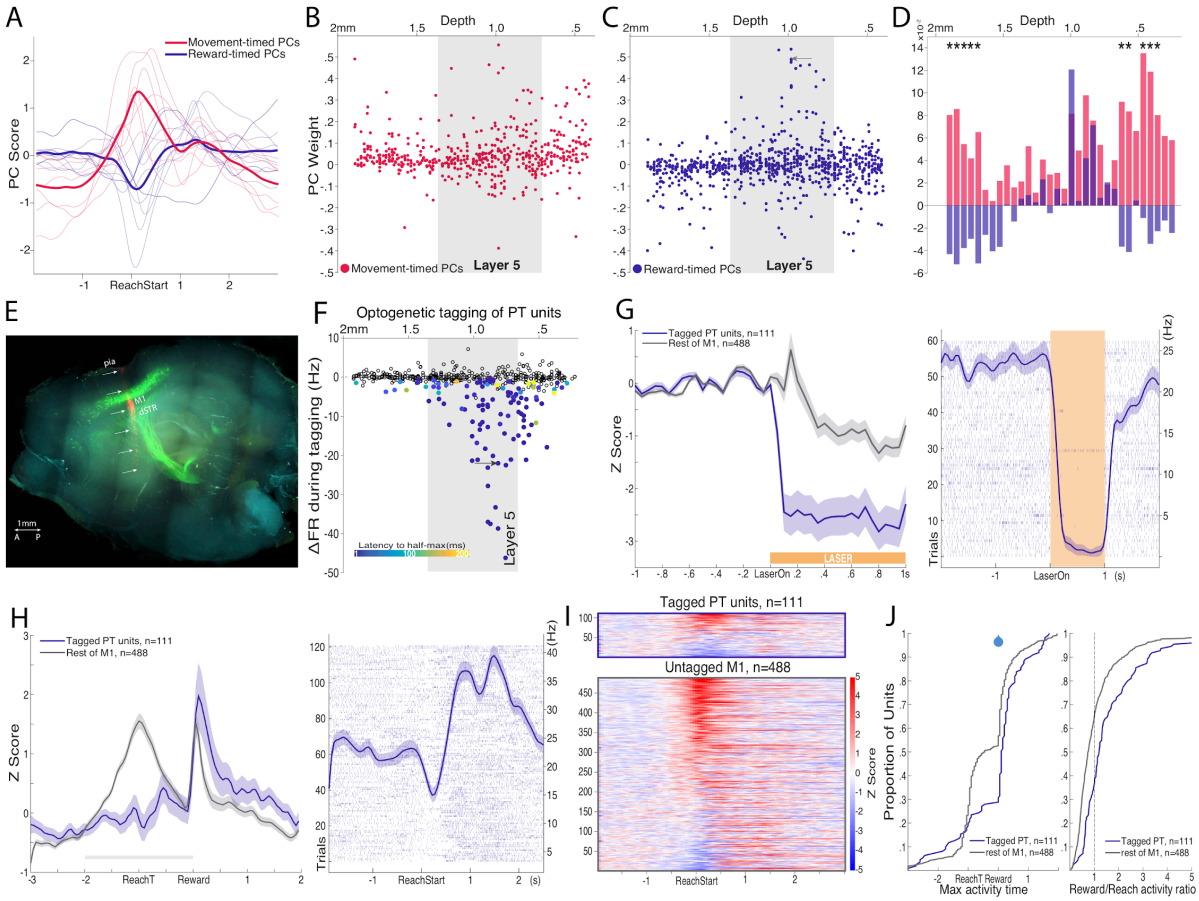

FIGURE 2

Encoding of kinematic variables is most prominent in superficial layer 5 of motor cortex

A) M1 neural activity projected onto the top three PCs (Methods). PCs are classified as 'Movement-timed' or 'Reward-timed' based on whether the PC scores peak before or after the +500 ms relative to the reach start.

B) Weights of the movement-timed PCs are plotted as a function of cortical depths of corresponding units.

C) Weights of the reward-timed PCs are plotted as a function of cortical depths of corresponding units.

D) Weights of movement- and reward-timed PCs appear to significantly differ across cortical depths.

E) Labelling of pons-projecting PT neurons (green) and the probe tract (red) with light sheet fluorescence microscopy on a cleared whole brain (see Supplemental Fig. 2 for more coronal and sagittal images). Scale bar=1mm.

F) Optogenetically tagged (filled circle) and untagged (empty circle) M1 units are plotted as a function of the recorded depth (x-axis) and the mean change of the firing rate (y-axis) with the latency of half-maximal firing rate inhibition color-coded. The arrow points to the example PT^{tag} unit shown in G and H.

G) *Left*, Normalized mean±SEM neural activity before and during optotagging. *Right*, The trial by trial activity (rasters, row per trial) of an example tagged unit exhibiting robust inhibition by laser (right, see Supplemental Fig. 3 for more examples). The mean±SEM spike rate (Hz) is superimposed.

H) *Left*, Normalized mean±SEM neural activity of tagged and untagged units during reaching and reward delivery. The superimposed gray bar marks time bins included in the statistical test. *Right*, Trial by trial activity (rasters) of the same PT^{tag} unit as in G aligned to the reach start with the mean±SEM spike rate superimposed. Note that trials with closed-loop laser stimulation were excluded in this plot and corresponding statistical analysis, thus the difference between PT^{tag} and the rest of M1 units is not due to the stimulation.

I) Normalized activity of all individual PT^{tag} and untagged units.

J) *Left*, A significantly greater portion of the PT^{tag} (70%) neuronal activity peaked after reward delivery compared to the rest (43%) of $MCtx^{FL}$ (χ^2_1=24.73, p=6.57x10^{-7}). *Right*, A significantly greater portion of the PT^{tag} (64%) neurons had a reward/reach activity ratio larger than 1, meaning a greater reward-timed activity, compared to the rest (35%) of $MCtx^{FL}$ (χ^2_1=30.93, p = 2.67x10^{-8}).

illumination onset (Fig. 2F-G, Supplemental Fig. 3; paired t-test, α=0.01). The vast majority of tagged PT units (PT^{tag}) were distributed at depths consistent with layer 5b (Fig. 2F; depth estimates from Allen Reference Atlas). These depths overlap with depths at which units with high loading coefficients in the reward-timed PC dimension were concentrated (Fig. 2C-D) providing further evidence that reward-timed activity is predominant in layer 5b PT neurons in this task.

We next compared the activity of the PT^{tag} neurons to activity from units throughout motor cortex aligned to reach-threshold crossing and reward. The modulation of activity in PT^{tag} population was significantly weaker than the rest of the cortical population during movement execution (Fig. 2H; group x time interaction; repeated measures ANOVA, $F_{1,40}$=11.82, p=1.66x10^{-74}, main effect of group; ANOVA, $F_{1,597}$=23.93, p=1.29x10^{-6}). Many of the putative PT neurons exhibited suppressed activity around reach start (Supplemental Fig. 3, left column). Excitatory modulation of activity, when apparent in a subset of putative PT neurons, tended to be delayed relative to movement initiation (Fig. 2J). These data suggest that the preparation and execution of self-initiated forelimb movements were only modestly accounted for by activity in the pons-projecting PT neurons of deep layer 5. In contrast, the clear tuning to movement kinematics and execution-related activity in more superficial and deeper populations of units in $MCtx^{FL}$ suggest that IT neuronal populations may be critical for movement execution. We note that IT neurons represent a significant fraction of corticostriatal projection neurons and that dSTR is critical for the modulation of movement vigor in this task[9,39] and many other tasks in diverse species[24,40,55].

Identifying cell-types via optogenetic tagging has been an important technique that has clarified cell-type specific basis of diverse neuronal correlates (e.g.[50]), however, it is also subject to well known limitations[17,49] - false negatives are particularly relevant in our study. Thus, we sought to use a complementary method to assess the cell-type specificity of $MCtx^{FL}$ activity in our task. We used cell type specific calcium imaging to more precisely target two major layer 5 neuron populations in $MCtx^{FL}$. Specifically, we focused on superficial layer 5 IT neurons that provide dense corticostriatal projections[37,56] and are localized in a region that appeared to have reliable movement-timed activity in our task (Fig. 1H, 2B)[26]. We used virally-driven expression of GCaMP6f in Sim1-cre and Tlx3-cre mice[17,54] which are known to preferentially drive expression of transgenes in deep layer 5b PT neurons and superficial layer 5a IT projection neurons, respectively (Fig 3A-D; Sim1-cre: 8 mice, 19 imaging sessions, N=1776 ROIs. Tlx3-cre: 7 mice, 14 imaging sessions, N=1006 ROIs)[17,54,56,57].

Overall the average PT and IT activity showed prominent differences that were consistent with the electrophysiology data. IT neurons showed substantially greater peri-movement activation than PT neurons, whilst PT neurons showed greater reward-timed and intertrial interval activity (Fig 3D). Analogous to the electrophysiological experiments we examined low dimensional activity using PCA. The first PC of population reflected a similar difference to that between PT and IT activity. Cells with a positive loading on to the first PC (PC1+) were characterized by prominent activation around movement execution and were more likely to be IT neurons. In contrast, cells with a negative loading (PC1-) were characterized by more reward-timed modulation of activity and were more likely to be PT neurons (Fig 3E-G, PT/IT difference on PC1: P<5.35x10^{-45}, Student's independent t-test).

Thus, cell-type specific two photon calcium imaging and large scale electrophysiology across cortical layers combined with optotagging both reveal that positively modulated movement-related signals are primarily in IT neurons of $MCtx^{FL}$, with PT neurons exhibiting more complex task related activity around delivery of rewards and between trials. We next sought to ask whether IT neurons in $MCtx^{FL}$ are indeed preferentially involved in controlling the amplitude of forelimb movements and better understand the interplay of IT and PT neurons during movement execution. We next revisited our optotagging data and an intriguing observation precipitated by combining large scale recordings across the cortical depth with cell-type specific perturbation (Fig. 4A). While we found that all units inhibited with short latency (half-maximal inhibition at 34±5 ms) were putatively localized to layer 5b, we also noticed that more superficially and deeper within MCtx as well as subcortically, many units were positively modulated at a relatively long latency (half-maximal excitation at 122±9 ms) after the onset of suppression of PT neuron activity (Fig.

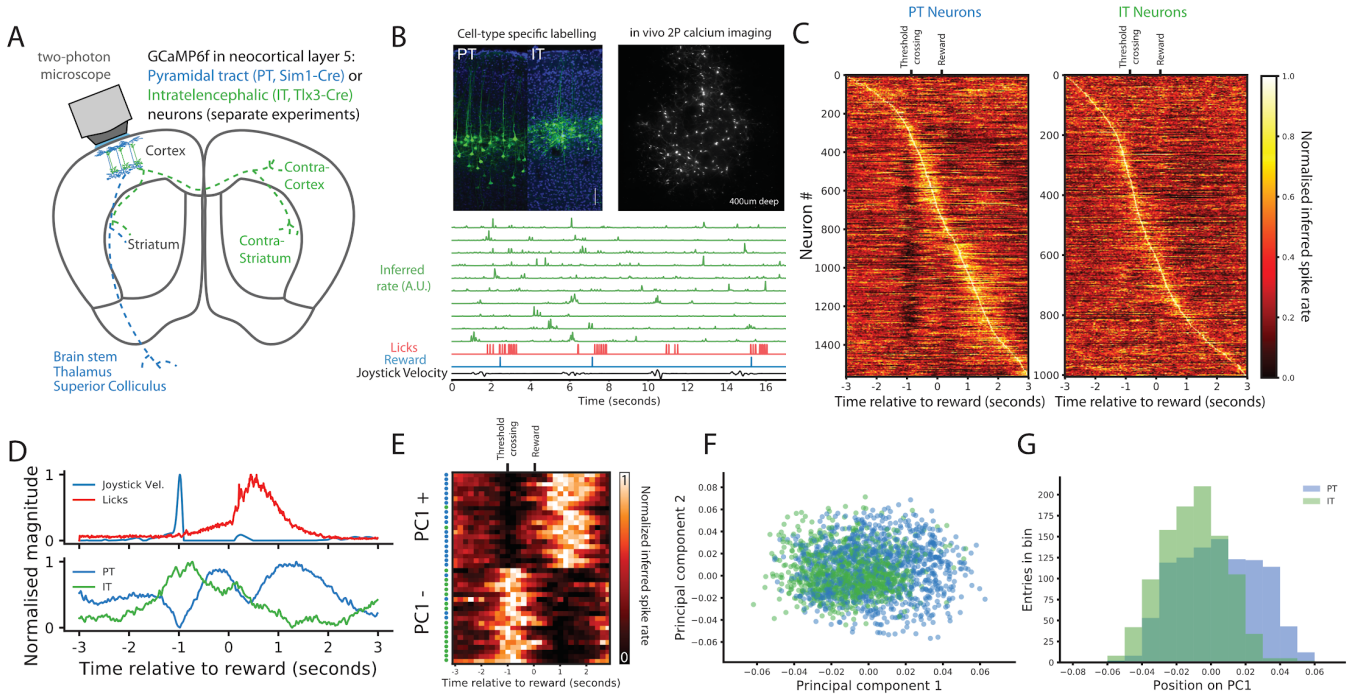

FIGURE 3
Cell-type specific imaging shows prominent movement-locked activity in IT neurons of motor cortex

A) Two-photon calcium imaging was performed from left MCtx^{FL}, targeting either layer PT or IT neurons (separate experiments). Schematic shows the different brain-wide targets of the two projections.
B) Top left: Histology from 2 imaged mice, one from each of the two mouse lines. Scale bar 100 microns, images are matched for scale. Top right: example field of view. Bottom row: behavioral variables aligned to example unit activity from an IT recording session. See, Supplemental Fig. 4 for examples of performance of the deconvolution algorithm.
C) Mean traces aligned to reward for every unit in the dataset, grouped by projection neuron type. Units are ranked by time of peak activity. Each row was normalized to range 0-1.
D) Top row shows the average joystick velocity (only showing velocity away from center) and lick rate. Bottom row shows mean PT and IT activity. All are aligned to reward delivery. IT neurons show prominent peri-movement activation, whilst PT peak activity occurs later. Units were mean averaged for each projection target, then resulting average was normalized to range 0-1.
E) Coloured dots on left reflect projection identity of unit. For PCA, PT units were randomly subsampled to match the size of IT population (using numpy random.choice function). The structures of individual principal components, and additional example units, are provided in Supplemental Fig. 5.
F) Unit weights on the first and second principal components, coloured as in A. Unit subset as in E.
G) Histogram of unit weights on principal component 1 for IT and PT neurons, with bin size 0.01.

4A, Supplemental Fig. 3 & 6; two-tailed independent t-test, $t_{223} = 8.17$, $p=2.36\times10^{-14}$). This observation highlights the complex interplay of activity amongst densely interconnected cell-types and the challenge of simple interpretations of cell-type specific optogenetic inactivation experiments.

Within MCtx^{FL} and in subcortical areas the subpopulation of units with delayed, 'paradoxical' excitation during optotagging procedure were the same units that exhibited preferential modulation of activity during movement (Fig. 4B-C, Supplemental Fig. 3, 6 & 7A-C; group x time interaction; repeated measures ANOVA, $F_{2,80} = 11.41$, $p=1.90\times10^{-138}$, main effect of group; ANOVA, $F_{2,596}=27.25$, $p=4.76\times10^{-12}$, pairwise test, $p<0.05$). The majority of the MCtx^{FL} units with delayed excitation (Fig. 4A & C, Supplemental Fig. 3; paired t-test, $\alpha=0.01$) were found in layers known to contain IT neurons and at depths similar to IT populations in the imaging data (Fig. 3). Moreover, the MCtx units that exhibited delayed excitation during optotagging were also units with the largest loading on to the movement-

timed PC dimension (Supplemental Fig. 7 & 8; pearson's correlation, r=0.31, p=2.7x10^{-12}). dSTR units that receive dense corticostriatal projections from IT neurons also exhibited similar delayed increases in activity (Fig. 4C, Supplemental Fig. 6) providing additional evidence that those units with paradoxical delayed excitation in response to PT suppression are most likely (a subpopulation of) IT neurons. Thus, we will refer to this subpopulation as 'IT^{pe}' units (Fig. 4A, Supplemental Fig. 3). Units with the characteristic robust, short latency inhibition will be referred to as the 'optotagged' PT^{tag} population (Fig. 4A, Supplemental Fig. 3 & 7).

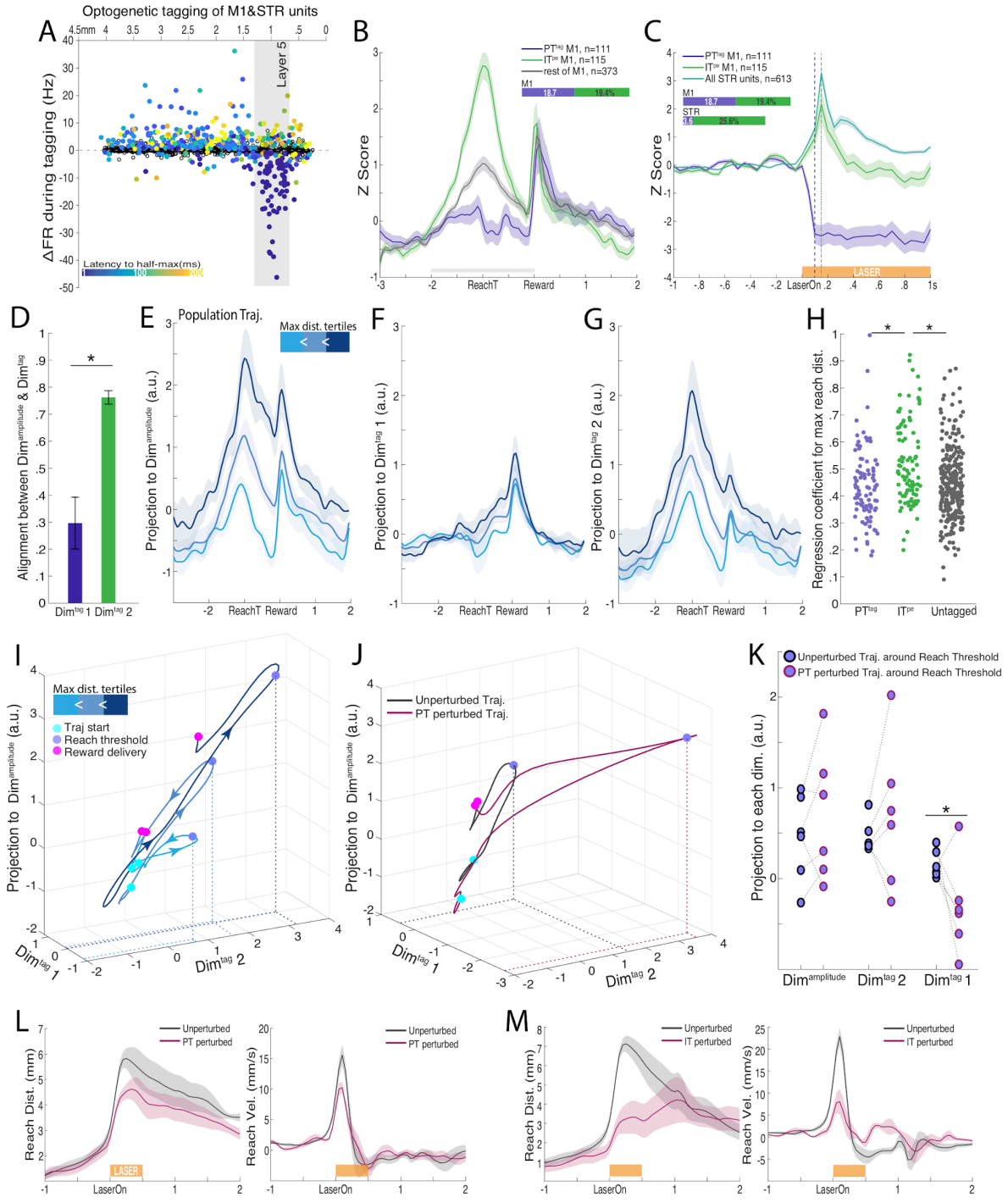

FIGURE 4
Movement-potent dimensions of population activity are preferentially composed of superficial layer 5 IT neurons in motor cortex

A) In contrast to fast and robust suppression of layer 5b neurons, optotagging positively modulated many non-layer 5b cortical and striatal neurons at a relatively long latency (half-maximal excitation at 122±9 ms after laser onset).
B) Normalized mean±SEM neural activity of PT^{tag}, IT^{pe}, and the rest of MCtx units during reaching and reward delivery. The superimposed gray bar marks time bins included in the statistical test. Note that trials with closed-loop laser stimulation were excluded in this plot and corresponding statistical analysis.
C) Normalized mean±SEM neural activity before and during optotagging. Superimposed stacked bars indicate MCtx and dSTR neuronal proportions with significant positive (green) or negative (blue) activity modulation during optotagging.
D) To examine how PT^{tag} and IT^{pe} neural population activity is related to movement-related MCtx activity, we measured how Dim^{tag} dimensions capturing inhibitory PT^{tag} and excitatory IT^{pe} optotagging responses were aligned to $Dim^{amplitude}$ dimension by taking the inner product between Dim^{tag} 1,2 and $Dim^{amplitude}$ dimension pair (perfect alignment = 1; orthogonal = 0).
E) Neural population trajectories across the reach-amplitude tertiles acquired by projecting MCtx neuronal activity onto $Dim^{amplitude}$ dimension.
F) Projection onto the Dim^{tag} 1 dimension (dimension capturing inhibitory - PT^{tag} primarily - optotagging responses), yielded neural trajectories modestly separable by reach amplitude.
G) Projection onto the Dim^{tag} 2 dimension (capturing excitatory - IT^{pe} primarily - responses), yielded distinct neural trajectories as a function of reach amplitude.
H) Regression coefficients of all individual PT^{tag}, IT^{pe}, and untagged units quantifying the linear relationship between the individual neuronal activity and reach amplitude across trials.
I) Neural trajectories of reach amplitude tertiles plotted along Dim^{tag} 2 (X axis), Dim^{tag} 1 (Y axis) and $Dim^{amplitude}$ (Z axis) dimensions, neural trajectories evolved along the unity line of the Dim^{tag} 2 and $Dim^{amplitude}$ dimensions as a function of reach amplitude, reiterating a high degree of alignment between the two. Note the modest excursion of neural trajectories along the Dim^{tag} 1 dimension.
J) Neural trajectories of unperturbed and closed-loop PT perturbation trials plotted along the same dimensions as in I. Note the sizable deviation of the neural trajectory by the optogenetic inactivation of PT neurons in negative and positive directions along the Dim^{tag} 1 and Dim^{tag} 2 dimensions, respectively.
K) Mean scores of projection onto $Dim^{amplitude}$, Dim^{tag} 2, and Dim^{tag} 1 dimensions (-0.5 to 0.5 s relative to reach threshold crossing) plotted for unperturbed and closed-loop PT perturbation trials of all six neural populations per recording session. Note the significant negative deviation along the Dim^{tag} 1 dimension in the closed-loop PT perturbation trials, reflecting inactivation of pons-projecting PT neurons (two-tailed independent t-test, $t_{10} = 2.24$, p=0.049). Along the Dim^{tag} 2 and $Dim^{amplitude}$ dimensions numerically positive deviations are observed in perturbation trials, which predicts modest behavioral impact of the PT perturbation (two-tailed independent t-test; $Dim^{amplitude}$, $t_{10} = 0.72$, p=0.49; Dim^{tag} 1, $t_{10} = 0.66$, p=0.53).
L) Mean±SEM reach distance (left) and velocity (right) of unperturbed (black) vs. PT perturbed (magenta) trials.
M) Mean±SEM reach distance (left) and velocity (right) of unperturbed (black) vs. IT perturbed (magenta) trials.

We next examined whether activity of this IT^{pe} population with robust movement-timed activity could be related to the control of movement kinematics by analyzing activity dynamics during movement execution. We first extracted dimensions that captured the variance in activity during the optotagging protocol (Dim^{tag}). In each data set, we found that the top two or three Dim^{tag} captured suppressed and enhanced components that reflected the sign of modulation of activity in the PT^{tag} and IT^{pe} populations, respectively (Supplemental Fig. 9). For clarity we refer to these principal components as the enhanced and suppressed 'Dim^{tag}' dimensions. The enhanced Dim^{tag} (IT^{pe}-related) dimension was positively correlated with the movement-timed PC, while the inhibitory Dim^{tag} (PT^{tag}-related) dimension was correlated with the reward-timed PC (Supplemental Fig. 8 top left & bottom right, respectively). The Dim^{tag} dimensions were also compared with the $Dim^{amplitude}$ dimension that best captured the neural variance as a function of reach amplitude. The enhanced Dim^{tag} dimension was more similar to $Dim^{amplitude}$ dimension compared to the suppressed Dim^{tag} dimension (inner product: 0.78 vs 0.15, respectively; Fig. 4D, two-tailed independent t-test, $t_6 = 3.61$, p=0.01).

These results suggest that the subpopulation of MCtx neurons paradoxically excited by PT suppression, is the same subpopulation that appears to dominate population activity dynamics that correlate with the kinematics of forelimb movements. This relationship was revealed in the trajectories of population activity for individual sessions. For example, the modulation of population activity obtained by projecting the $MCtx^{FL}$ population activity onto the enhanced Dim^{tag} 2 dimension increased systematically in proportion to movement amplitude (Fig. 4E-G, ANOVA, $F_{2,15} = 9.96$, $p=1.8x10^{-3}$). In contrast, population trajectories within the inhibitory Dim^{tag} 1 dimension revealed much smaller differences as a function of amplitude (Fig. 4F, ANOVA, $F_{2,15} = 3.56$, p=0.054). Consistent with this interpretation, IT^{pe} units had systematically larger regression coefficients relating trialwise modulation of activity to movement amplitude compared to the PT^{tag} units or the rest of the $MCtx^{FL}$ population (Fig. 4H, ANOVA, $F_{2,457} = 13.06$, $p=3.04x10^{-6}$).

To directly compare dynamics along the dimensions identified from optogenetic tagging periods outside the task with the dimension of activity best correlated with reach amplitude during task, we plotted dynamics along Dim^{tag} dimensions against $Dim^{amplitude}$ dimension (Fig 4I-J). We found that the enhanced Dim^{tag} 2 and $Dim^{amplitude}$ dimensions were highly correlated (Fig. 4I) whereas the suppressed Dim^{tag} 1 and $Dim^{amplitude}$ dimensions were largely independent (Fig. 4I; example population with N=129 units). These data suggest that the enhanced Dim^{tag} 2 dimension is a 'movement-potent' dimension related to the control of movement amplitude, whereas the orthogonal Dim^{tag} 1 dimension reflects a 'movement-null' dimension in the context of this task[32]. Previous work has argued that population activity in primate MCtx during a pre-movement (preparatory) period was inferred to be movement-null because no movement was observed and the population activity during execution was primarily along an orthogonal dimension[32] - an observation consistent with theoretical predictions[58]. However, one test of this model currently lacking experimental support is that perturbation of activity specifically along the movement-null dimension during execution should produce little modulation of movement kinematics.

We next sought to test this prediction by using closed-loop, cell-type specific perturbation of activity in $MCtx^{FL}$ populations selectively during movement execution. If it is the case that the suppressed Dim^{tag} 1 dimension (PT^{tag}-dominated activity) is primarily along a movement-null dimension, then this perturbation should have little effect on movement execution. We first confirmed that perturbation during movement produced large modulation of population activity primarily along the suppressed Dim^{tag} 1 (PT^{tag}-related) dimension with more modest modulation along the enhanced Dim^{tag} 2 (IT^{pe}-related) dimension as predicted (Fig. 4J-K). Finally, we examined its effect on movement kinematics. Suppression of pons-projecting PT neuron activity during movement had a small effect on the amplitude and speed of forelimb movements (Fig. 4L, ANOVA, amplitude; $F_{1,10} = 3.80$, p=0.080; speed; $F_{1,10} = 2.78$, p=0.127). Thus, these data provide strong evidence that the dimension of population activity dominated by pons-projecting PT-type projection neurons is, at least in this task, a movement-null dimension contrary to expectations from other tasks [5,17] (we should note however that previous work has not evaluated the causal contribution of PT neurons to execution).

These results also make another strong prediction: the population we identify functionally as IT^{pe}, which we have argued is likely a subset of IT neurons, should make a critical contribution to movement-potent dimensions. To assess this prediction we performed cell-type specific inactivation of STR-projecting IT neurons (see Methods). As predicted, perturbation of the IT population had large effects on movement kinematics (Fig. 4M, ANOVA, amplitude; $F_{1,12} = 17.34$, p=0.001; speed; $F_{1,12} = 10.98$, p=0.006). We note that this occurred despite the much smaller number of neurons expressing the optogenetic inhibitor (FLInChR[53]) in the IT population. The fact that perturbation experiments allow a dramatic change in the relative contribution of PT neurons during movement execution without altering kinematics suggests that cortical motor commands can be routed to downstream targets in a flexible and cell-type selective manner depending on the specific demands of the task.

Discussion

We trained mice to flexibly regulate the vigor (amplitude) with which they displaced a spring-loaded joystick while making large scale population

recordings throughout all layers of motor cortex and dorsal through ventral striatum - major telencephalic structures for the control of limb movements. We observed a clear encoding of movement amplitude in mouse forelimb motor cortex and, as previously described[9,40], in dorsal striatum. Surprisingly, both large scale electrophysiology with optotagging of neuron subtypes and imaging of targeted cell types revealed that the representation of movement kinematics was predominantly observed in layer 5 IT populations and much reduced in deep layer 5 pons-projecting PT neurons. This result is in contrast to the suggestion that for cortically-dependent movements motor commands are conveyed primarily via PT neurons[5,16]. However, our observations are consistent with key roles for subcortical structures such as basal ganglia in the regulation of movement vigor[39,59], critical functions for extrapyramidal motor pathways in regulating movement execution[60], and the notion that corticospinal projections are primarily recruited for fine control of dexterity [2,61] rather than gross movement[59]. Our data together with previous work provide evidence that the relative recruitment of IT and PT neuron types is task specific and reflects a flexible routing of motor cortical output through downstream effectors[17].

Many studies of cortical encoding of movement have focused on cued movements of individual limbs along highly stereotyped trajectories, whereas here we studied a self-paced bimanual task in which mice were adapting the vigor of movements. IT neurons are a distinct class of projection neuron characterized by dense interhemispheric projections [38,62,63] and bimanual movements appear to require coordination of activity across hemispheres in rodents [64]. IT neurons are also a major source of cortical input to striatum (IT is often synonymous with corticostriatal[26,37,56,62]) which is known to be important for self-initiated actions and the control of movement vigor[24,55,65]. Thus, several pieces of behavioral evidence are consistent with this task robustly engaging IT neurons. We note that previous studies have observed movement execution related activity in IT neuron populations during movements in primates as well[26]. Our data suggest that circuit mechanisms underlying cortical control of movement in other species may also be further elucidated by using tasks with diverse features (*e.g.* self-initiation, bimanual, adapting vigor).

The notion that MCtx population activity can be substantially perturbed in ways that directly alter movement and those that are largely inconsequential for overt movement has been long standing[11]. Indeed, this idea is central to account for preparatory activity in primary motor areas [31,32] and complex functional-tuning between individual neurons and the muscles they innervate [11,66]. One formulation of this idea is movement-potent vs movement-null dimensions of population activity [4,18,32,58]. However, to date it has been unknown how activity in defined cell-types relates to population activity broadly and to null and potent dimensions specifically[7]. A common assumption is that PT output activity must be aligned with a movement-potent dimension across diverse tasks [5]. However, tests of this point have been lacking because cell-type specific perturbations must be combined with large scale recording to connect population activity to the causal contributions of individual cell types. Here we overcame this limitation and combined optogenetic suppression of a specific projection cell types (*e.g.* pons-projecting PT neurons) during a rest period with closed-loop perturbation during movement execution in the same recording sessions. We found that selective suppression of PT neuron activity during rest produced large perturbations of population activity that were in fact aligned with a movement-null dimension identified during movement execution. This point is made concrete by observing that suppression of PT neurons during movement execution had little effect on movement kinematics despite producing large changes to population activity. Thus, cortically-dependent movements with highly similar kinematics can be controlled with varying amounts of PT neuron activity.

Here we suggest that flexible routing through output pathways (*e.g.* the ratio of IT to PT activity during movement execution) may be conceptualized as changing the position of MCtx activity along a movement-null dimension. The relative contribution of PT neuron activity to movement execution may thus vary substantially across tasks or contexts without directly altering the gross kinematics of the underlying movement, but perhaps being scaled in proportion to demands for dexterity [2,59]. Large-scale recording across layers shows that complex recurrent dynamics can adjust

the balance of these two major projection pathways on a millisecond timescale and thus allow for robust cortical control of movement. We suggest that this provides a circuit mechanism by which actions have both abstract (kinematic) representations and can realize those kinematic representations through varying configurations of descending projection neuron cell types[5].

References

1. Churchland, M. M. *et al.* Neural population dynamics during reaching. *Nature* **487**, 51–56 (2012).
2. Sauerbrei, B., Guo, J. Z., Mischiati, M., Guo, W. & Kabra, M. Motor cortex is an input-driven dynamical system controlling dexterous movement. *bioRxiv* (2018).
3. Peters, A. J., Chen, S. X. & Komiyama, T. Emergence of reproducible spatiotemporal activity during motor learning. *Nature* **510**, 263–267 (2014).
4. Li, N., Daie, K., Svoboda, K. & Druckmann, S. Robust neuronal dynamics in premotor cortex during motor planning. *Nature* **532**, 459–464 (2016).
5. Miri, A. *et al.* Behaviorally Selective Engagement of Short-Latency Effector Pathways by Motor Cortex. *Neuron* **95**, 683–696.e11 (2017).
6. Michaels, J. A., Dann, B. & Scherberger, H. Neural Population Dynamics during Reaching Are Better Explained by a Dynamical System than Representational Tuning. *PLoS Comput. Biol.* **12**, e1005175 (2016).
7. Sussillo, D., Churchland, M. M., Kaufman, M. T. & Shenoy, K. V. A neural network that finds a naturalistic solution for the production of muscle activity. *Nat. Neurosci.* **18**, 1025–1033 (2015).
8. Anderson, C. T., Sheets, P. L., Kiritani, T. & Shepherd, G. M. G. Sublayer-specific microcircuits of corticospinal and corticostriatal neurons in motor cortex. *Nat. Neurosci.* **13**, 739–744 (2010).
9. Panigrahi, B. *et al.* Dopamine Is Required for the Neural Representation and Control of Movement Vigor. *Cell* **162**, 1418–1430 (2015).
10. Brown, J., Martin, K. A. & Dudman, J. Behavioral evidence for feedback gain control by the inhibitory microcircuit of the substantia nigra. *bioRxiv* (2016).
11. Lemon, R. N. Descending pathways in motor control. *Annu. Rev. Neurosci.* **31**, 195–218 (2008).
12. Mazzoni, P., Hristova, A. & Krakauer, J. W. Why don't we move faster? Parkinson's disease, movement vigor, and implicit motivation. *J. Neurosci.* **27**, 7105–7116 (2007).
13. Tresilian, J. R. & Stelmach, G. E. Common organization for unimanual and bimanual reach-to-grasp tasks. *Exp. Brain Res.* **115**, 283–299 (1997).
14. Vargas-Irwin, C. E. *et al.* Decoding complete reach and grasp actions from local primary motor cortex populations. *J. Neurosci.* **30**, 9659–9669 (2010).
15. Shmuelof, L. & Krakauer, J. W. Are we ready for a natural history of motor learning? *Neuron* **72**, 469–476 (2011).
16. Economo, M. N. *et al.* Distinct descending motor cortex pathways and their roles in movement. *Nature* **563**, 79–84 (2018).
17. Li, N., Chen, T.-W., Guo, Z. V., Gerfen, C. R. & Svoboda, K. A motor cortex circuit for motor planning and movement. *Nature* **519**, 51–56 (2015).
18. Shenoy, K. V., Sahani, M. & Churchland, M. M. Cortical control of arm movements: a dynamical systems perspective. *Annu. Rev. Neurosci.* **36**, 337–359 (2013).
19. Barrett, D. G., Denève, S. & Machens, C. K. Optimal compensation for neuron loss. *Elife* **5**, (2016).
20. Kawai, R. *et al.* Motor cortex is required for learning but not for executing a motor skill. *Neuron* **86**, 800–812 (2015).
21. Lawrence, D. G. & Kuypers, H. G. The functional organization of the motor system in the monkey. I. The effects of bilateral pyramidal lesions. *Brain* **91**, 1–14 (1968).
22. Lawrence, D. G. & Kuypers, H. G. The functional organization of the motor system in the monkey. II. The effects of lesions of the descending brain-stem pathways. *Brain* **91**, 15–36 (1968).
23. Xu, J., Haith, A. M. & Krakauer, J. W. Motor Control of the Hand Before and After Stroke. *Clinical Systems Neuroscience* 271–289 (2015). doi:10.1007/978-4-431-55037-2_14
24. Dudman, J. T. & Krakauer, J. W. The basal ganglia: from motor commands to the control of vigor. *Curr. Opin. Neurobiol.* **37**, 158–166 (2016).
25. Fetz, E. E. Cortical mechanisms controlling limb movement. *Curr. Opin. Neurobiol.* **3**, 932–939 (1993).
26. Turner, R. S. & DeLong, M. R. Corticostriatal activity in primary motor cortex of the macaque. *J. Neurosci.* **20**, 7096–7108 (2000).
27. Moran, D. W. & Schwartz, A. B. Motor cortical representation of speed and direction during reaching. *J. Neurophysiol.* **82**, 2676–2692 (1999).
28. Georgopoulos, A. P., Schwartz, A. B. & Kettner, R. E. Neuronal population coding of movement direction. *Science* **233**, 1416–1419 (1986).
29. Maier, M. A., Shupe, L. E. & Fetz, E. E. Recurrent neural networks of integrate-and-fire cells simulating short-term memory and wrist movement tasks derived from continuous dynamic networks. *J. Physiol. Paris* **97**, 601–612 (2003).
30. Fetz, E. E. & Shupe, L. E. NEURAL NETWORK MODELS OF THE PRIMATE MOTOR SYSTEM. *Advanced Neural Computers* 43–50 (1990). doi:10.1016/b978-0-444-88400-8.50009-1
31. Churchland, M. M., Cunningham, J. P., Kaufman, M. T., Ryu, S. I. & Shenoy, K. V. Cortical preparatory activity: representation of movement or first cog in a dynamical machine? *Neuron* **68**, 387–400 (2010).
32. Kaufman, M. T., Churchland, M. M., Ryu, S. I. & Shenoy, K. V. Cortical activity in the null space: permitting preparation without movement. *Nat. Neurosci.* **17**, 440–448 (2014).

33. Chen, S. X., Kim, A. N., Peters, A. J. & Komiyama, T. Subtype-specific plasticity of inhibitory circuits in motor cortex during motor learning. *Nat. Neurosci.* **18**, 1109–1115 (2015).
34. Huber, D. *et al.* Multiple dynamic representations in the motor cortex during sensorimotor learning. *Nature* **484**, 473–478 (2012).
35. Peters, A. J., Lee, J., Hedrick, N. G., O'Neil, K. & Komiyama, T. Reorganization of corticospinal output during motor learning. *Nature Neuroscience* **20**, 1133–1141 (2017).
36. Shepherd, G. M. G. Corticostriatal connectivity and its role in disease. *Nat. Rev. Neurosci.* **14**, 278–291 (2013).
37. Dudman, J. T. & Gerfen, C. R. The basal ganglia. *The Rat Nervous System (Fourth Edition)* (2015).
38. Spruston, N., Svoboda, K. & Chandrashekar, J. Reconstruction of 1,000 projection neurons reveals new cell types and organization of long-range connectivity in the mouse brain. (2019).
39. Yttri, E. A. & Dudman, J. T. Opponent and bidirectional control of movement velocity in the basal ganglia. *Nature* **533**, 402–406 (2016).
40. Yttri, E. A. & Dudman, J. T. A proposed circuit computation in basal ganglia: History-dependent gain. *Mov. Disord.* (2018).
41. Znamenskiy, P. & Zador, A. M. Corticostriatal neurons in auditory cortex drive decisions during auditory discrimination. *Nature* **497**, 482–485 (2013).
42. Lee, A. M., Tai, L.-H., Zador, A. & Wilbrecht, L. Between the primate and 'reptilian' brain: Rodent models demonstrate the role of corticostriatal circuits in decision making. *Neuroscience* **296**, 66–74 (2015).
43. Jun, J. J. *et al.* Fully integrated silicon probes for high-density recording of neural activity. *Nature* **551**, 232–236 (2017).
44. Mante, V., Sussillo, D., Shenoy, K. V. & Newsome, W. T. Context-dependent computation by recurrent dynamics in prefrontal cortex. *Nature* **503**, 78–84 (2013).
45. Zhao, S. *et al.* Cell type–specific channelrhodopsin-2 transgenic mice for optogenetic dissection of neural circuitry function. *Nat. Methods* **8**, 745 (2011).
46. Bollu, T. *et al.* Automated home cage training of mice in a hold-still center-out reach task. *J. Neurophysiol.* **121**, 500–512 (2019).
47. Guo, J.-Z. *et al.* Cortex commands the performance of skilled movement. *Elife* **4**, e10774 (2015).
48. Subramaniam, R., Kardon, B. M., Cohen, I. & Goldberg, J. H. Motor cortical inactivation reduces the gain of kinematic primitives in mice performing a hold-still center-out reach task. *BioRxiv* (2018).
49. Lima, S. Q., Hromádka, T., Znamenskiy, P. & Zador, A. M. PINP: a new method of tagging neuronal populations for identification during in vivo electrophysiological recording. *PLoS One* **4**, e6099 (2009).
50. Cohen, J. Y., Haesler, S., Vong, L., Lowell, B. B. & Uchida, N. Neuron-type-specific signals for reward and punishment in the ventral tegmental area. *Nature* **482**, 85–88 (2012).
51. Pan, W.-X., Brown, J. & Dudman, J. T. Neural signals of extinction in the inhibitory microcircuit of the ventral midbrain. *Nat. Neurosci.* **16**, 71–78 (2013).
52. Tervo, D. G. R. *et al.* A Designer AAV Variant Permits Efficient Retrograde Access to Projection Neurons. *Neuron* **92**, 372–382 (2016).
53. Brown, J. *et al.* Expanding the Optogenetics Toolkit by Topological Inversion of Rhodopsins. *Cell* **175**, 1131–1140.e11 (2018).
54. Gerfen, C. R., Paletzki, R. & Heintz, N. GENSAT BAC cre-recombinase driver lines to study the functional organization of cerebral cortical and basal ganglia circuits. *Neuron* **80**, 1368–1383 (2013).
55. Turner, R. S., Desmurget, M., Grethe, J., Crutcher, M. D. & Grafton, S. T. Motor subcircuits mediating the control of movement extent and speed. *J. Neurophysiol.* **90**, 3958–3966 (2003).
56. Hooks, B. M. *et al.* Topographic precision in sensory and motor corticostriatal projections varies across cell type and cortical area. *Nat. Commun.* **9**, 3549 (2018).
57. Chen, T.-W. *et al.* Ultrasensitive fluorescent proteins for imaging neuronal activity. *Nature* **499**, 295–300 (2013).
58. Druckmann, S. & Chklovskii, D. B. Neuronal circuits underlying persistent representations despite time varying activity. *Curr. Biol.* **22**, 2095–2103 (2012).
59. Lemke, S. M., Ramanathan, D. S., Guo, L., Won, S. J. & Ganguly, K. Emergent modular neural control drives coordinated motor actions. *Nat. Neurosci.* (2019). doi:10.1038/s41593-019-0407-2
60. Wang, Z., Maunze, B., Wang, Y., Tsoulfas, P. & Blackmore, M. G. Global Connectivity and Function of Descending Spinal Input Revealed by 3D Microscopy and Retrograde Transduction. *J. Neurosci.* **38**, 10566–10581 (2018).
61. Gu, Z. *et al.* Control of species-dependent cortico-motoneuronal connections underlying manual dexterity. *Science* **357**, 400–404 (2017).
62. Greig, L. C., Woodworth, M. B., Galazo, M. J., Padmanabhan, H. & Macklis, J. D. Molecular logic of neocortical projection neuron specification, development and diversity. *Nature Reviews Neuroscience* **14**, 755–769 (2013).
63. Tasic, B. *et al.* Shared and distinct transcriptomic cell types across neocortical areas. *Nature* **563**, 72–78 (2018).
64. Igarashi, M. The role of interhemispheric cortico-cortical connections in bimanual coordination in the rat. (2019).
65. Klaus, A., Alves da Silva, J. & Costa, R. M. What, If, and When to Move: Basal Ganglia Circuits and Self-Paced Action Initiation. *Annu. Rev. Neurosci.* **42**, 459–483 (2019).
66. Griffin, D. M., Hoffman, D. S. & Strick, P. L. Corticomotoneuronal cells are 'functionally tuned'. *Science* **350**, 667–670 (2015).

67. Osborne, J. E. & Dudman, J. T. RIVETS: a mechanical system for in vivo and in vitro electrophysiology and imaging. *PLoS One* **9**, e89007 (2014).
68. Arenkiel, B. R. *et al.* In vivo light-induced activation of neural circuitry in transgenic mice expressing channelrhodopsin-2. *Neuron* **54**, 205–218 (2007).
69. Madisen, L. *et al.* A toolbox of Cre-dependent optogenetic transgenic mice for light-induced activation and silencing. *Nat. Neurosci.* **15**, 793–802 (2012).
70. Tennant, K. A. *et al.* The organization of the forelimb representation of the C57BL/6 mouse motor cortex as defined by intracortical microstimulation and cytoarchitecture. *Cereb. Cortex* **21**, 865–876 (2011).
71. Harrison, T. C., Ayling, O. G. S. & Murphy, T. H. Distinct cortical circuit mechanisms for complex forelimb movement and motor map topography. *Neuron* **74**, 397–409 (2012).
72. Goldey, G. J. *et al.* Removable cranial windows for long-term imaging in awake mice. *Nat. Protoc.* **9**, 2515–2538 (2014).
73. Podgorski, K. & Ranganathan, G. Brain heating induced by near-infrared lasers during multiphoton microscopy. *J. Neurophysiol.* **116**, 1012–1023 (2016).
74. Packer, A. M., Russell, L. E., Dalgleish, H. W. P. & Häusser, M. Simultaneous all-optical manipulation and recording of neural circuit activity with cellular resolution in vivo. *Nat. Methods* **12**, 140–146 (2015).
75. Theis, L. *et al.* Benchmarking Spike Rate Inference in Population Calcium Imaging. *Neuron* **90**, 471–482 (2016).
76. Kubota, S. I. *et al.* Whole-Body Profiling of Cancer Metastasis with Single-Cell Resolution. *Cell Rep.* **20**, 236–250 (2017).
77. Yu, B. M. *et al.* Gaussian-Process Factor Analysis for Low-Dimensional Single-Trial Analysis of Neural Population Activity. *Journal of Neurophysiology* **102**, 614–635 (2009).

ACKNOWLEDGEMENTS
The authors thank Brett Mensh and Jason Keller for comments on earlier drafts of the manuscript. The authors thank several members of Janelia Research Campus for assistance with experimental hardware. For Neuropixels recordings Brian Barbits, Jennifer Colonel, Tim Harris, James Jun, Bill Karsh, Wei-Lung Sun, and Eric Yttri provided critical assistance in developing the recording system and associated hardware. For imaging experiments Dan Flickinger provided key assistance in the design of the microscope. Janelia Viral Tools and Vivarium provided critical support for these experiments. A.W.H. is a Group Leader and J.T.D. is a Senior Group Leader at Janelia Research Campus of the Howard Hughes Medical Institute (HHMI). This work was supported by funding from HHMI.

METHODS

Male and female mice, typically aged 8-16 weeks at time of surgery, were used in this study. All procedures were approved by the Janelia Research Campus Institutional Animal Care and Use Committee (IACUC) and were consistent with the standards of the Association for Assessment and Accreditation of Laboratory Animal Care. Mice were water restricted (1-1.2ml water/day), and their weight and signs of health were monitored daily as in[9].) Surgical methods closely followed those previously described[9,67] except where indicated below.

Behavior

Behavioral code was implemented as described previously[9] and run from a microcontroller based system (details can be obtained from http://dudmanlab.org/html/resources.html). After surgery (see below), mice were given 5 days of recovery prior to beginning water restriction (1ml water/day). Following 3-5 days of initial water restriction, they underwent 10-20 days training, which simply involved exposure to the task and self-learning. Mice were head-fixed in a custom made head restraint box using the RIVETS head-fixation apparatus (see Osborne & Dudman, 2014 for methods[67]). The mouse's front paws rested on a metal bar attached to a spring-loaded joystick, which had unconstrained 2D maneuverability in the horizontal plane. Mice were trained to maneuver the joystick to certain thresholds varying across three different blocks (e.g. 3-4-3 mm) to obtain a sweetened water reward delivered 1 s after each threshold crossing. Rewards were followed by a 3 s inter-trial interval (ITI) in which no movements would be rewarded. There were up to 150 trials (50 trials per block) in electrophysiology and 120 trials per session in imaging (some sessions were incomplete), with one water reward being available per trial. All behavioral events (forelimb movements, licks) were recorded on separate channels at 25 kHz (USB-6366; National Instruments, Austin, Texas) then downsampled offline at 1 kHz. Forelimb movements were assessed offline to detect individual reaches based on the velocity joystick movement. Time points of reach start and stop were defined as well as other kinematic properties such as duration, maximum amplitude and velocity for each reach.

Extracellular electrophysiological identification and recording of FLInChR-expressing neurons in awake mice

For cell-type specific in vivo recordings from motor cortex and striatum, rAAV2-retro-CAG-Flex-FLInChR-mVenus (3.0E+12 GC/ml) was injected to the pons bilaterally (relative to lambda: 0.4 mm anterior, 0.4 mm lateral, 5.5, 5.75, 6 mm deep, 70 nL/depth) in Sim1-cre (KJ18Gsat) mice, selectively labeling a pyramidal type (PT) layer 5 population [16,52,54]. Prior to recordings, a craniotomy was made over the recording sites (relative to bregra: 0.5 mm anterior, 1.7mm lateral) at least 12 hours prior to recording under isoflurane anaesthesia. Exposed brain tissue was kept moist with phosphate-buffered saline at all times, and craniotomy sites were covered with Kwik-Sil elastomer (WPI) outside of the recording session.

For neural population recording using the Neuropixels probe [43], awake mice fully recovered from craniotomy were head-fixed in a RIVETS chamber [67]. A Neuropixels probe (option 3 phase A) with 374 recording sites was briefly (~2 minutes) dipped into the dil cell-labeling solution (ThermoFisher) to visualize probe tracks, then lowered through the craniotomy manually. After a slow, smooth descent (200 mm/min), the probe sat still at the target depth for at least 5 min before initiation of recording to allow the electrodes to settle. An Ag wire was soldered onto the reference pad of the probe and shorted to ground. This reference wire was connected to an Ag/AgCl wire was positioned on the skull. The craniotomy and the Ag/AgCl wire were covered with a saline bath. Voltage signals are filtered (high-pass above 300 Hz), amplified (200x gain), multiplexed and digitized (25 kHz) on the base, allowing the direct transmission of noise-free digital data from the probe, and were recorded using an open-source software SpikeGLX (https://github.com/billkarsh/SpikeGLX). Recorded data were pre-processed using an open-source software JRCLUST (https://github.com/JaneliaSciComp/JRCLUST) to identify single- or multi units in the primary motor cortex (M1) and STR. To assay FLInChR expression and responses, a fiber (200 mm core, 0.39 NA, Thorlabs) coupled to a 574 nm laser source (Omicron) was placed to deliver light onto the craniotomy. Single laser pulses of 1 s duration with power measured at the tip of the fiber of 4-8 mW were delivered 60 times with 8 s intervals.

Cell-type specific closed-loop perturbation of M1 neuronal activity

To examine the cell-type specific role of the deep layer 5 PT neurons in MCtx, we injected rAAV2-retro-CAG-Flex-FLInChR-mVenus[52,53] into the pons (relative to lambda: 0.4 mm anterior, 0.4 mm lateral, 5.5, 5.75, 6 mm deep, 70 nL/depth) in three Sim1-cre (KJ18Gsat[54]) mice. Viruses obtained from Janelia Viral Tools (https://www.janelia.org/support-team/viral-tools). To examine the role of the IT neurons in MCtx, we bilaterally injected the same virus into the dorsal striatum (relative to bregma: 0.5 mm anterior, 1.6 mm lateral, 2, 2.7, 3.5 mm deep, 150 nL/depth) and cortex (site 1 : 0.9 anterior, 1.5 lateral, site 2: 0.1 anterior, 1.9 lateral, site 3: 0.1 anterior, 1.1 lateral, each site at 300+600 microns deep, 80nl/depth) in five Tlx3-cre (PL56Gsat[54]), respectively. In closed-loop experiments, a 500 ms single pulse of 574 nm laser was delivered bilaterally in randomly selected 30 % of the trials immediately when mice moved the joystick by 1.5mm from the zero point taken at the end of each ITI.

To examine the general role of MCtx in control of forelimb movement regardless of the projection neuronal cell-type, we implanted optical fibers (200 mm core, 0.39 NA, Thorlabs) bilaterally to place fiber tips right onto the pia of the brain in VGAT-ChR2-eYFP[68] (Fig 1) or Rbp4-cre[54]::Ai32[69] (Extended Data Fig 1) mice. In closed-loop experiments, a 500 ms single pulse of 473 nm laser was delivered in randomly selected trials triggered by a slight joystick movement caused by mice. In open-loop experiments, a 3 s single pulse of 473 nm laser was delivered in randomly selected 30 % of trials at a given time point (2 s after previous reward delivery during inter-trial interval in select trials) regardless of animals' behavior.

Cell-type specific two-photon calcium imaging

Viruses were AAV 2/1-Flex-GCaMP6f, diluted to $2*10^{12}$gc/ml [57] and obtained from Janelia Viral Tools (https://www.janelia.org/support-team/viral-tools). 5 injections performed in a cross-shape, centered on 1.6 lateral, 0.6 rostral. 20nL was ejected at 600um depth. This center was chosen based upon previous microstimulation work[70,71]. Imaging was restricted to one month after injection to minimise overexpression.

3mm-wide circular imaging windows were made over the left cortical hemisphere in all animals, following the method of Goldey *et al*[72]. Window implants were centered on the virus injection center, and fixed in place using cyanoacrylate glue and dental acrylic. Windows (custom ordered from Potomac photonics) were made by placing three windows together, with the top window being 3.5mm, the bottom two being 3mm, such that the top window rested on thinned skull area. This triple window arrangement was used to increase downward pressure on the brain and stabilize the brain motion.

Imaging was performed with a custom built two photon laser scanning microscope running scanImage software (latest versions, from 2013-2016; https://vidriotechnologies.com). GCaMP6f was excited with a ti:sapphire laser, tuned to 920nm. Imaging was typically performed at 33Hz via bidirectional scanning with a resonant galvo. Power at sample did not exceed 150mW. In poorer quality windows, frame rate was halved to allow an increase in peak pulse power. This was done to minimise photodamage from thermal effects [73]. Depth of recording ranged from 350um-450um, depending upon imaging clarity, corresponding to the proximal dendritic region of the apical dendrite.

All imaging data analysis was performed in Python using custom-written scripts unless otherwise stated. Imaging data was motion corrected in two stages. Firstly, an image average was taken for a session across all frames. Secondly, each frame was then motion registered to that image, based upon a Fourier-based cross-correlation approach to detect the optimal corrective displacement. The average was then re-taken, and the process repeated 3 times. The result of this image registration process was examined by eye for each session to check for errors.

Region of interest (ROI) extraction was done manually in imageJ software. ROIs with high baseline fluorescence, a putative marker for unhealthy cells, were not used[74]. Fluorescence traces were deconvolved to inferred rates using published code[75]. We note that this is not an attempt to claim specific firing rates of neurons, but rather to reduce the distorting effect of the calcium sensors' slow kinetics on the inferred activity. We did not attempt to calibrate these inferred spike rates with real rates.

Histology

Fluorescence light sheet microscopy of cleared mouse whole brain

At completion of all electrophygiological experiments, mice were perfused with 40 ml of cold PBS (pH 7.4) containing 20 U/ml heparin at ~10ml/min, and fixed with cold 4% PFA. Extracted brains were further fixed for 24hrs in 4% PFA. Fixed brains were delipidated using the CUBIC-L cocktail 10 w%/10w% N-butyldiethanolamine/Triton X-100 for a week. Delipidated brains underwent nuclear counterstaining with TO-PRO-3 (ThermoFisher) for a day. We then transparentized the delipidated brains in the refractive index (RI) matching cocktail CUBIC-R composed of 45 w%/30 w% antipyrine/nicotinamide for two days [76]. Finally, cleared brains were imaged using fluorescence light sheet microscopy (Zeiss Lightsheet Z.1) to visualize expression of FLInChR (509 nm), probe tracks (570 nm), and nuclear counterstaining (661 nm).

DATA ANALYSIS METHODS

Neural data analysis

Single unit data analyses and statistical tests were performed using custom-written codes in Matlab. Spikes of isolated single units in M1 and striatal areas were counted within 1-ms bins to generate the trial-by-bin spike count matrix per unit aligned to reach start or reward delivery. The trial-averaged firing rates were calculated within 50-ms bins and z-score normalized using the mean and standard deviation of its baseline (a 2500-ms period before reach start) firing rate.

Dimensionality reduction (PCA)

To find the direction along which the neural population activity most covaried during task performance and extract low dimensional neural population trajectories along these directions, PCA was performed on a data matrix D of size (bt, n), where b and t are the number of 50-ms time bins and the number of trials, respectively, n is the number of neurons. The trial-by-trial binned spike counts are square-root transformed to construct D [77]. Applying PCA to D obtain X and W such that X = DW, where X is the projection of the data onto the principal components (PCs), which are orthonormal columns comprising W that contains the weights from neurons to PCs. To reveal the time-evolving patterns of population activity, $D_{t,b}$ were projected onto top three PCs, trial-averaged and strung together across time to generate neural population trajectories on each PC dimension versus time (Fig. 2A). PCA was also performed on the neural population activity during the optotagging protocol after completion of task performance to identify dimensions that capture neural activity covariance during optical inactivation of pons-projecting PT neurons. The top two or three PCs from each dataset reflected the fast suppression and delayed paradoxical activation of putative PT and IT neurons in MCtx (Extended Data Fig. 9). To compare the PCs derived from

the optotagging protocol (Dim^{tag}) with PCs extracted from activity during movement execution within the task, we measured Pearson correlation between PCs (Extended Data Fig. 8).

Targeted dimensionality reduction

To quantify representation of reach amplitude by the MCtx neural population we used a targeted dimensionality reduction [44] method. The goal was to identify the dimension (axis) within the state space of length N_{unit} defined by the activity of each unit, which account for neural response variance related to movement kinematic variables such as reach amplitude, velocity, and the number of licking.

The analysis comprised three steps. First, we conducted PCA to denoise the population responses and focus our analyses on the subspace spanned by the first ten PCs [1,77]. A data matrix X of size (ct, n) comprised averaged population responses corresponding to tertiles of three relevant movement kinematic variables - reach amplitude, velocity, and lick count, where c and t were all possible 27 combinations of the three movement kinematic variable tertiles and the number of 50-ms time bins, respectively, n was the number of neurons. The PCs of this data matrix are vectors a of length N_{unit}, and the denoising matrix D was built using the first ten PCs, where D=a=110aaT (see the denoised regression vectors defined below).

We used a multiple linear regression to quantify how much the activity of each unit varied as a function of movement kinematic variables:

ri,t(k)=i,t(1)amplitude(k)+i,t(2)velocity(k)+i,t(3)lick(k)+i,t(4), (eq. 1),

where ri,t(k)is the z-scored response of unit i at time t on trial k, amplitude(k), velocity(k), lick(k) are the maximum reach amplitude, reach velocity, and the number of licking on trial k discretized as tertiles of all trials in each behavioral session, e.g. for amplitude(k), 1, 2, 3 were assigned to trials of low, medium, high reach amplitudes. The last regression coefficient captures variance that is independent of the movement kinematic variables. The regression coefficients i,t(v) indicate how much the trial-by-trial firing rate of unit i at a given time t during the trial, can be regressed onto each movement kinematic variable . To estimate the regression coefficients i,t(v), a design matrix Fi of size Ncoef×Ntrialcomprising values for each movement kinematic regressor across trials was built for each recorded unit i. The regression coefficients were then estimated as:

i,t=(FiFiT)-1Firi,t.

We use the regression coefficients i,t estimated for individual units to identify dimensions within state space along which the neural population activity most covaried with movement kinematic variables. For each task variable, a 'regression vector' v,t of length N_{unit} is obtained whose entries v,t(i) correspond to regression coefficients for kinematic variable , time t, and unit i. Regression coefficient vectorsv,t(i) are then denoised by projecting them into the subspace spanned by the first ten PCs using the denoising matrix D defined above:

v,tpca=Dβv,t,

Time-independent denoised regression vectors vmax are then obtained by identifying the time at which the denoised regression vectors have maximum norm.

vmax=v,tvmaxpca with

tvmax=argmaxtv,tpca,

Finally, we obtain orthogonal axes in state space corresponding to neural variance associated with movement kinematic variables by orthogonalizing vmax with QR decomposition:

Bmax=QR,

where Bmax=[amplitudemax velocitymax lickmax]is a matrix whose columns are the time-independent denoised regression vectors vmax. The first three columns of Qcorrespond to the orthogonalized regression vectors v which we refer to as the movement kinematic axes, $Dim^{amplitude}$, $R^{velocity}$, and R^{lick} of length N_{unit}. Projection onto these axes reveal neural population activity as a function of movement kinematics (Fig. 1D, 4E-G).

To focus on the neural population variance as a function of reach amplitude avoiding the issue of multicollinearity between movement kinematic variables in the linear regression model, we repeated targeted dimensionality reduction with only replacing *eq. 1* with *eq. 2* below with the rest of the analysis kept identical:

ri,t(k)=i,t(1)amplitude(k)+i,t(2), (eq. 2).

Targeted dimensionality reduction using the two regression models identified almost identical axes as $Dim^{amplitude}$, and thus the projection scores appeared to be similar. Figures represent the result using *eq. 2*.

Supplemental videos:

Supplemental video 1. Example trials with/without closed-loop inactivation of MCtxFL neural activity by activation of inhibitory neurons in VGAT-ChR2 mice.
(Left) A representative trial with closed-loop inactivation of MCtxFL. A filled circle in the upper left corner indicates frames with laser on. Numbers in the bottom left corner indicate time relative to the laser onset triggered by slight movement of the animal. Video replay is at x0.2 speed.
(Right) A representative trial without closed-loop inactivation. An empty circle in the upper left corner indicates frames for which laser would have been delivered. Numbers in the bottom left corner indicate time relative to the pseudo laser onset.

Video 1 can be found online at: https://www.dropbox.com/s/vy6dzrqwm4w1eix/Trial%2354_139_stim-Pstim%20%28Converted%29.mov?dl=0

Supplemental Figures:

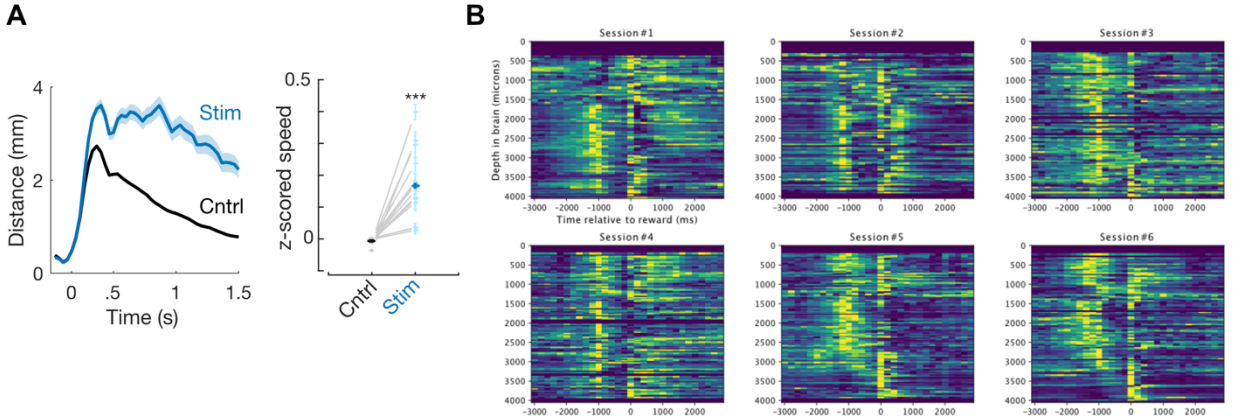

Supplemental Figure 1.
Supplemental from Figure 1. **A** Closed loop stimulation of the majority of descending layer 5 output neurons in MCtx^{FL} labelled using the Rbp4-cre line [54,63] crossed to Ai32[69] produced increases in the vigor of movement (see Fig. 1E). **B** Individual session data from Fig. 1F.

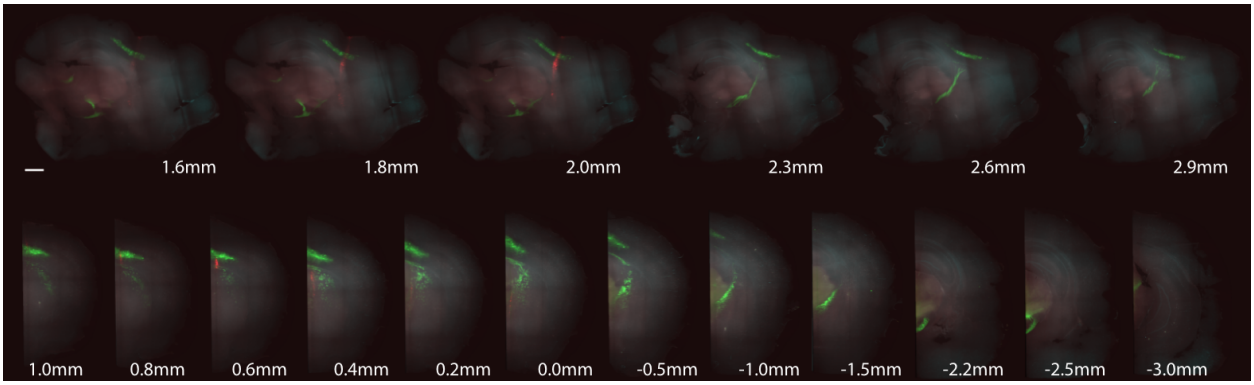

Supplemental Figure 2.
A sagittal (top row) and coronal (bottom row) view of a mouse hemi-brain.
Green fluorescence indicates labeling of the deep layer 5 PT neurons and their projections to downstream areas such as striatum, superior colliculus and pons. Red fluorescence indicates probe tracks. Numbers in the top and bottom rows indicate medial-lateral and anterior-posterior coordinates relative to bregma, respectively. The length of the white scale bar = 1mm.

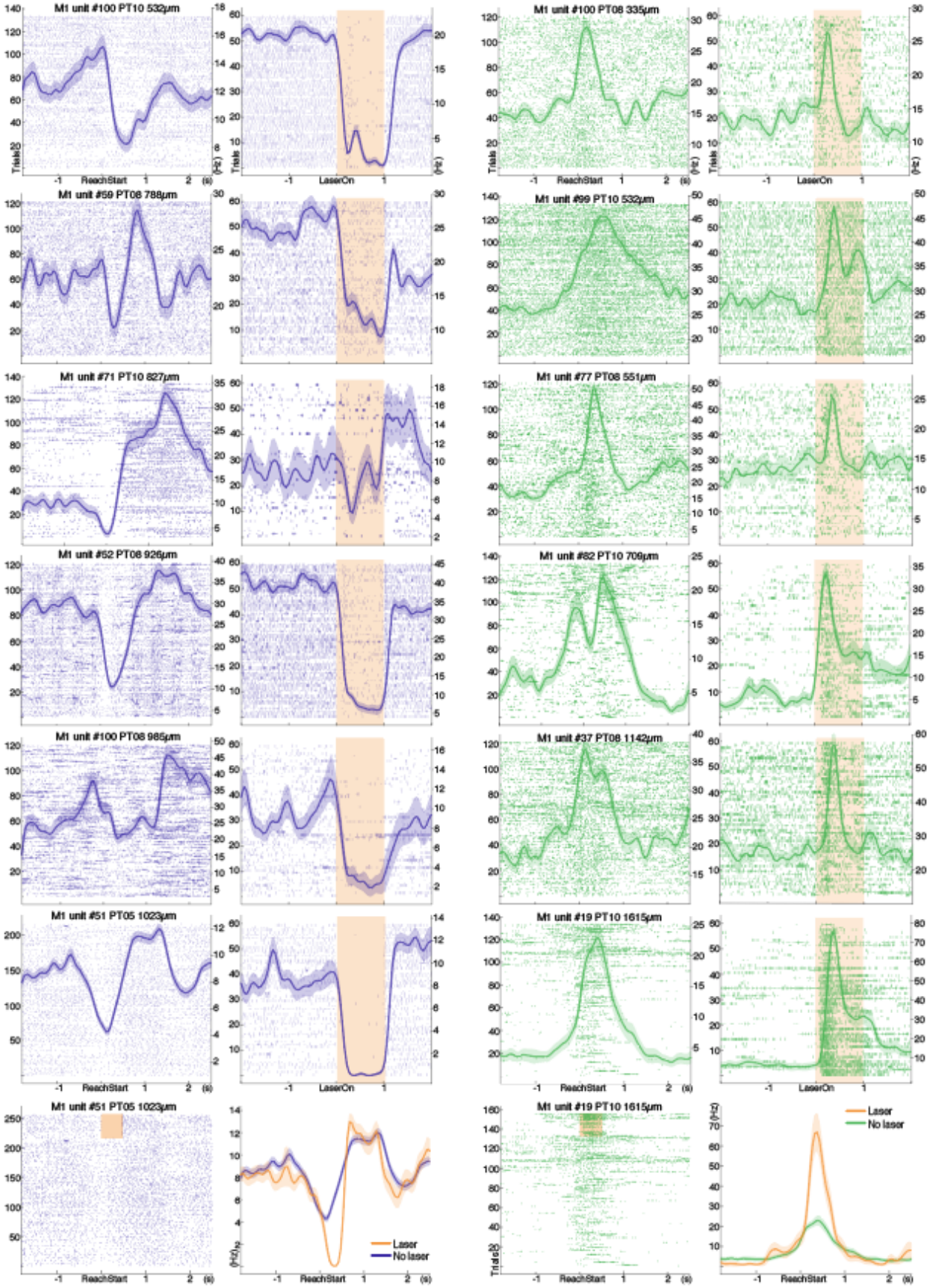
M1 unit #100 PT10 532µm
M1 unit #100 PT08 335µm
M1 unit #59 PT08 788µm
M1 unit #99 PT10 532µm
M1 unit #71 PT10 827µm
M1 unit #77 PT08 551µm
M1 unit #52 PT08 926µm
M1 unit #82 PT10 709µm
M1 unit #100 PT08 985µm
M1 unit #37 PT08 1142µm
M1 unit #51 PT05 1023µm
M1 unit #19 PT10 1615µm
M1 unit #51 PT05 1023µm
M1 unit #19 PT10 1615µm
Trials
(Hz)
ReachStart
LaserOn
(s)
Laser
No laser

Supplemental Figure 3.
Individual MCtx neuronal responses during task performance and optotagging. Blue-colored rasters in the left column illustrate trial by trial individual neuronal responses during task performance (left panel of each pair, aligned to reach start) with significant inhibitory responses during optotagging (right panel of each pair, aligned to laser onset) in Sim1-Cre (KJ18Gsat) mice injected with rAAV2-retro-CAG-Flex-FLInChR-mVenus to the pons. Each row represents each trial. The mean±SEM spike rate (Hz) is superimposed. Numbers on the left and right ordinates of each plot indicate the number of trial and firing rate in Hz, respectively. Note the immediate and robust inhibition during optotagging displayed by the PT^{tag} units recorded from the deep layer 5 (estimated recording depths at the top of each plot) in MCtx. Green-colored rasters in the right column illustrate trial by trial individual neuronal responses during task performance (left panels) and optotagging (right panels). Note the delayed and transient paradoxical excitation during optotagging displayed by the IT^{pe} units recorded from outside of the deep layer 5 in MCtx. The bottom row illustrates two example neuronal responses during reaches (same units from the above row) with or without the closed-loop perturbation, indicating consistent effects of perturbation during movement and rest. Top rows of the raster plots correspond to trials with laser.

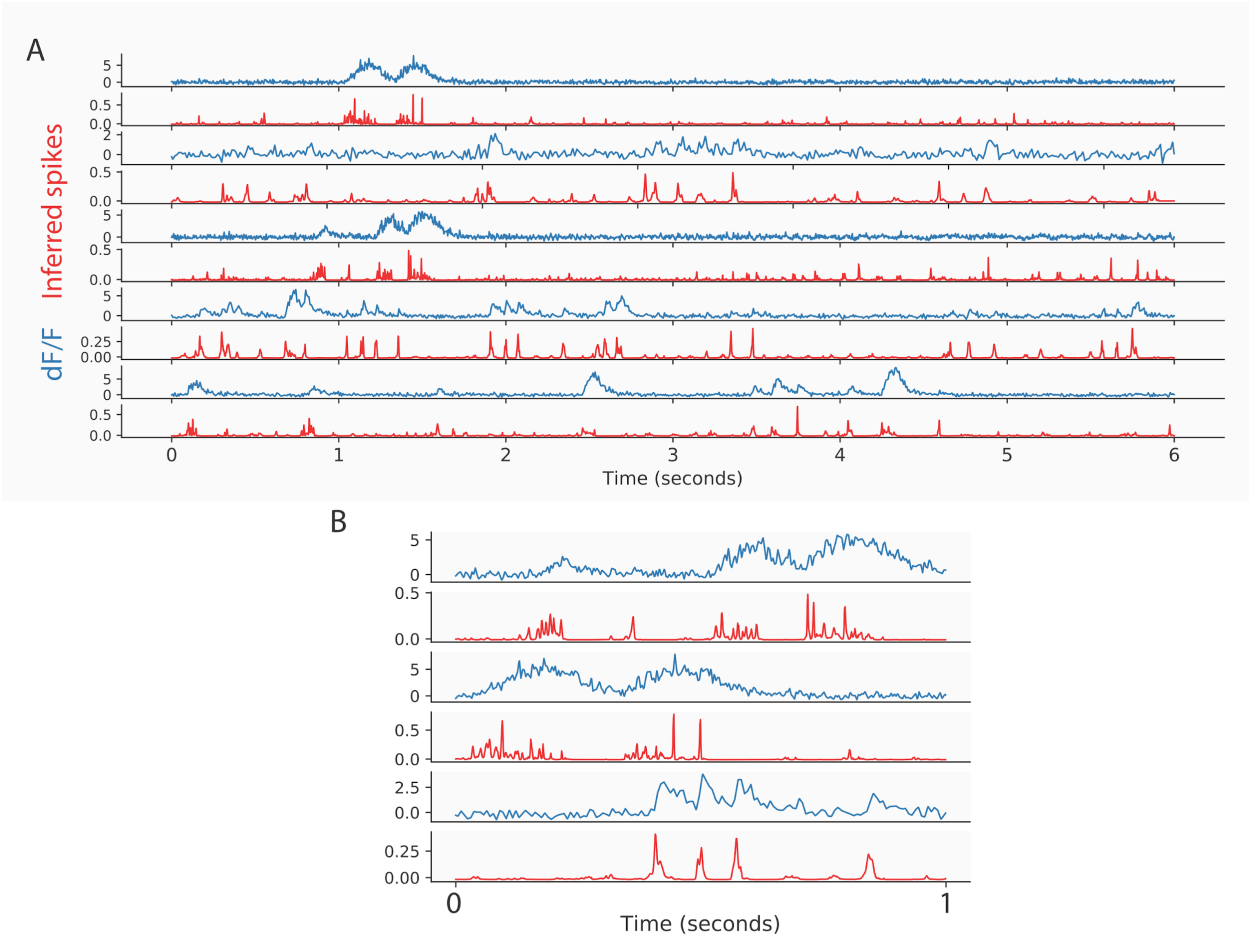

Supplemental Figure 4.
Examples of spike deconvolution performance.

A) Illustration of spike deconvolution. Panel shows 5 example regions of interest, each of two rows. Top row for each unit (blue) shows the dF/F trace, with the row beneath (red) showing the inferred spike activity metric.
B) Shows a zoomed-in portion for three units from A.

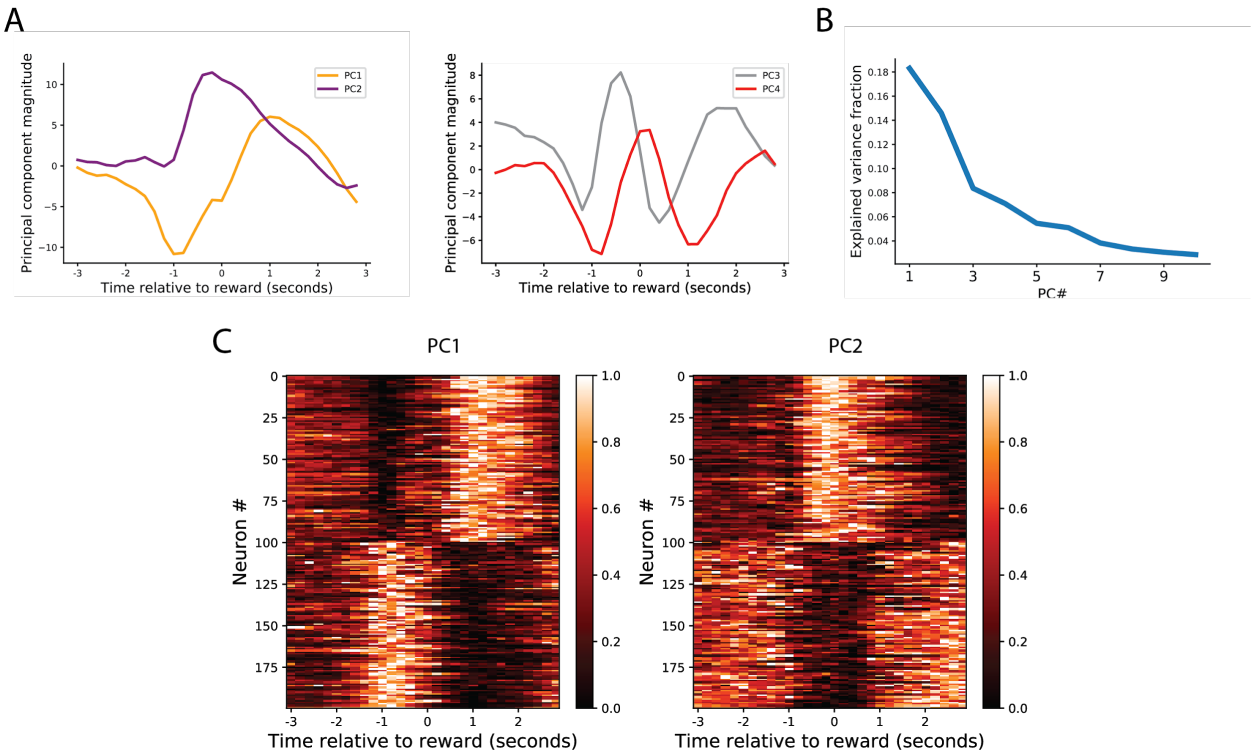

Supplemental Figure 5
Further information about Imaging data principal components

A. Structure of first four principal components of neural activity across all units in the dataset, aligned to reward.
B. The fraction of explained variance for the top 10 principal components in the dataset (same as B.)
C. Same as in Fig 3E, but for for a larger number of units and for PC2 as well. Top 100 units are the most positively weighted units on PC1 (left) and PC2 (right), bottom 100 units are the most negatively weighted units.

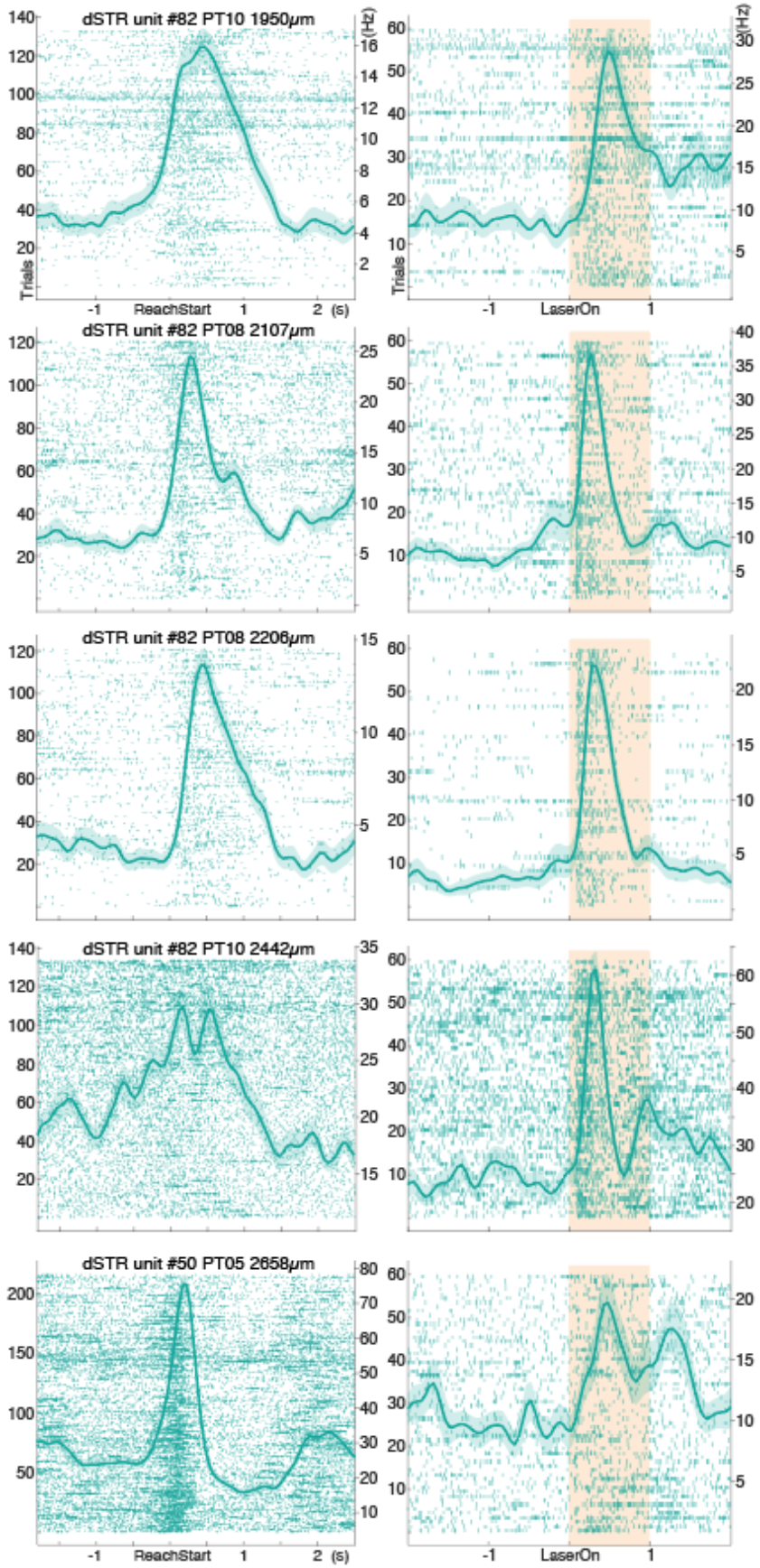
dSTR unit #82 PT10 1950μm
dSTR unit #82 PT08 2107μm
dSTR unit #82 PT08 2206μm
dSTR unit #82 PT10 2442μm
dSTR unit #50 PT05 2658μm
Trials
(Hz)
ReachStart
LaserOn
(s)

Supplemental Figure 6.
Individual dSTR neuronal responses during task performance and optotagging
Rasters in the left column illustrate trial by trial individual neuronal responses during task performance (left panel of each pair, aligned to reach start) and optotagging (right panel of each pair, aligned to laser onset) in Sim1-Cre (KJ18Gsat) mice injected with rAAV2-retro-CAG-Flex-FLInChR-mVenus to the pons. Format same as Supplemental Fig 3.
Note the delayed and transient excitation during optotagging displayed by the striatal units similar to that of the IT^{pe} units shown in Supplemental Fig 3.

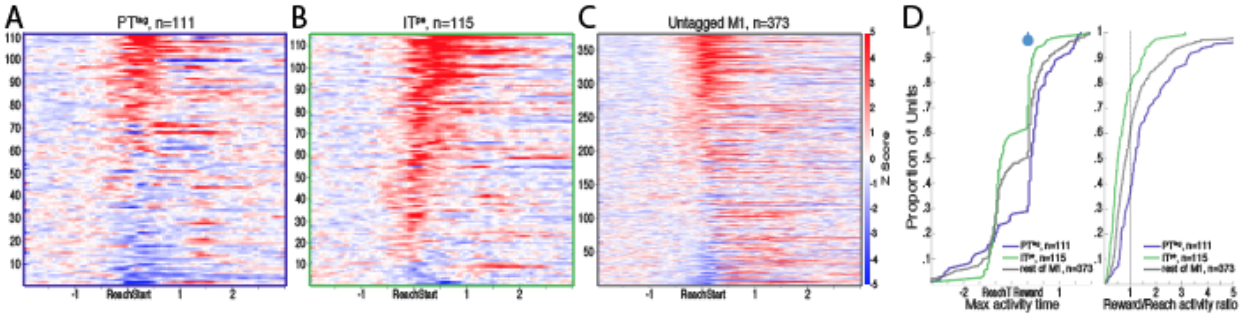

Supplemental Figure 7.
Distinct responses of PT^{tag} and IT^{pe} units during forelimb reach
A-C) Trial-averaged z-scored activity of individual PT^{tag} (A) and IT^{pe} (B) units, and the rest of M1 units (C) aligned to reach start.
D) Left, Cumulative distribution of the peak time of neuronal activation plotted separately for PT^{tag}, IT^{pe}, and the rest of the M1 subgroups. Note that the majority of the IT^{pe} units peaked before reward delivery, whereas the activity of the majority of the PT^{tag} units peaked after reward delivery. Right, Cumulative distribution of the reward/reach ratio plotted separately for PT^{tag}, IT^{pe}, and the rest of the M1 subgroups. IT^{pe} units exhibited relatively greater reach-timed responses, whereas PT^{tag} units displayed greater reward-timed responses.

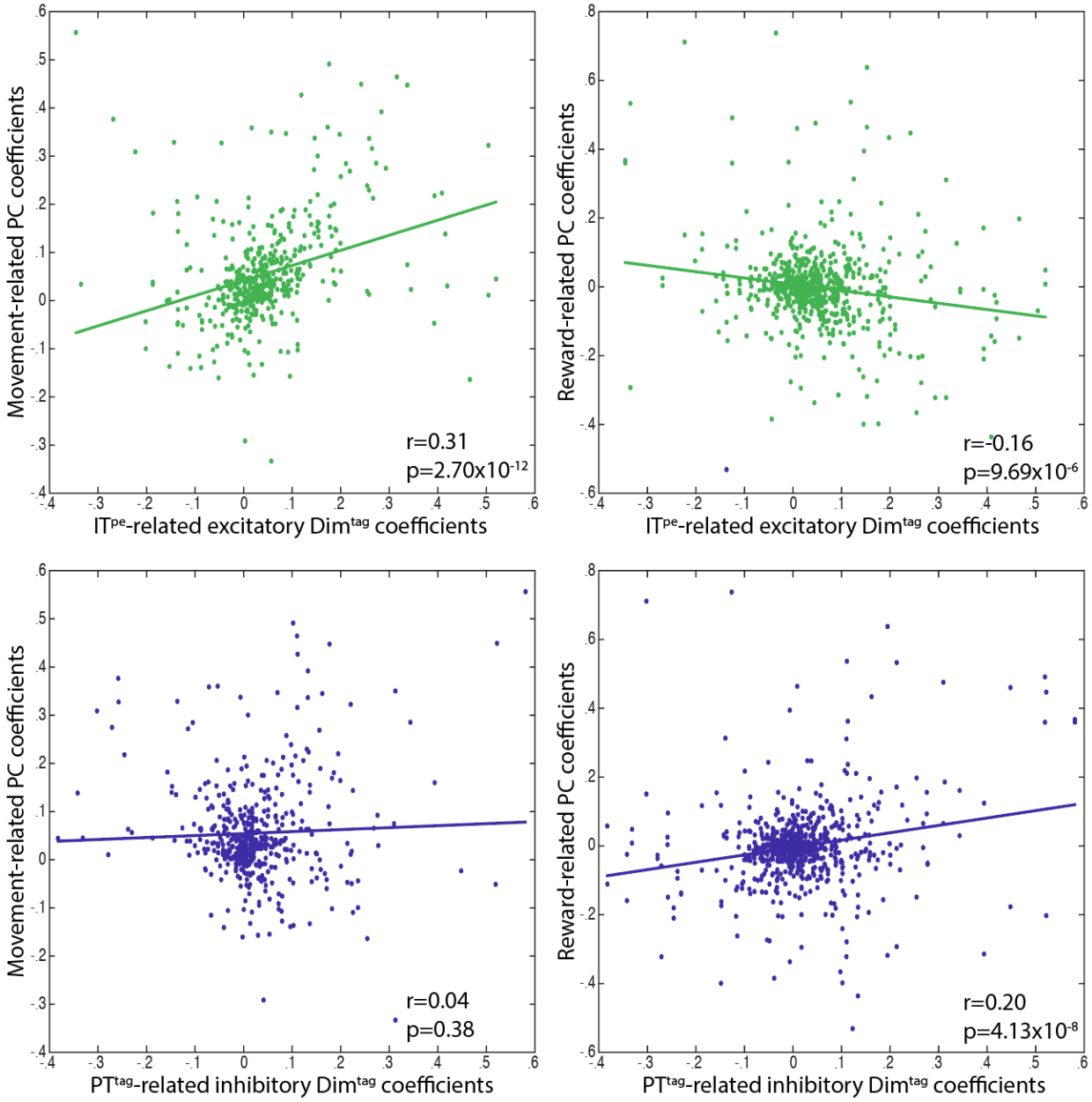

Supplemental Fig 8. Relationship between principal dimensions extracted from task performance and optotagging neural activity.
Separate PCAs were run on neural population activity during task performance and during optotagging to identify principal dimensions of length N_{unit} along which the neural population activity most covaried during each period. The forelimb movement-related PC coefficients show a significant positive correlation with the IT^{pe}-related excitatory Dim^{tag} coefficients (upper left panel). Intuitively, this positive relationship indicates IT^{pe} neurons, which showed paradoxical excitatory responses during optotagging outside of the deep layer 5 in M1, are heavily involved in the forelimb movement task. By contrast, the IT^{pe}-related excitatory Dim^{tag} coefficients show a negative correlation with the reward-related PC coefficients (upper right panel). PT^{tag}-related inhibitory Dim^{tag} coefficients, which captured the inhibitory responses of PT neurons during optotagging, show a significant positive correlation with the reward-related PC coefficients (bottom right panel). Intuitively, this positive

relationship indicates involvement of tagged PT neurons in the reward-timed responses, but not movement-time responses as no significant relationship is found between PT^{tag}-related inhibitory Dim^{tag} coefficients and movement-related PC coefficients (bottom left panel).

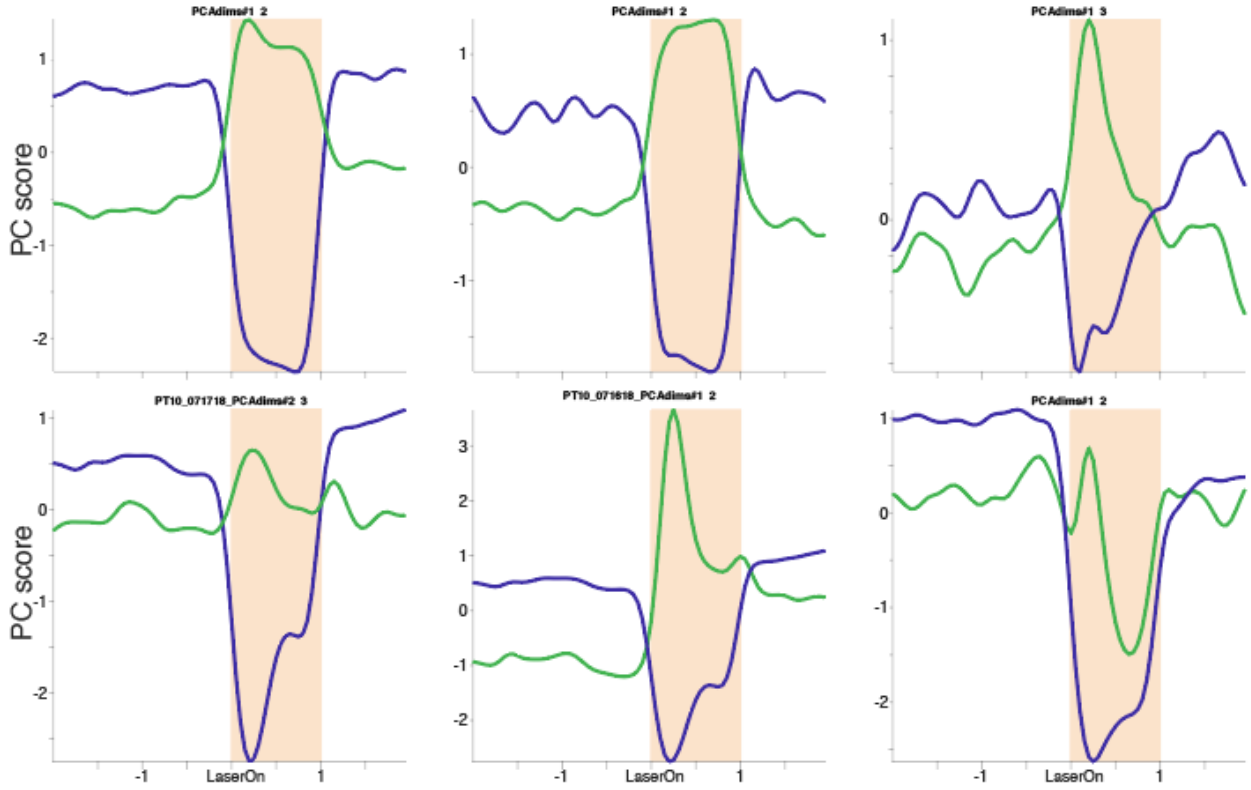

Supplemental Fig 9. Top principal components (Dim^{tag}) capture the suppressed and enhanced optotagging responses from PT^{tag} and IT^{pe} neural populations.
Top two or three PCs per each recording session extracted by PCA run on neural responses during optotagging captured the inhibitory (blue) PT^{tag} and excitatory (green) IT^{pe} MCtx neural responses in Sim1-Cre (KJ18Gsat) mice injected with rAAV2-retro-CAG-Flex-FLInChR-mVenus to the pons. This together with the individual neuronal responses during optotagging shown in Fig. 2G, 4A, Supplemental Fig. 3 & 6 illustrate robust and extensive impact of cell-type specific PT neuronal inactivation in the entire layers of MCtx and even in striatum.